Graded BMP Signaling Within Intestinal Crypt Architecture Directs Self-organization of the Wnt-secreting Stem Cell Niche

Judith Kraiczy[1,2], **Neil McCarthy**[1,2,#], **Ermanno Malagola**[3,#], **Guodong Tie**[1], **Shariq Madha**[1], **Dario Boffelli**[4], **Daniel E. Wagner**[5], **Timothy C. Wang**[3], **Ramesh A. Shivdasani**[1,2,6,*]

[1]Department of Medical Oncology and Center for Functional Cancer Epigenetics, Dana-Farber Cancer Institute, Boston, MA 02215, USA

[2]Departments of Medicine, Brigham & Women's Hospital and Harvard Medical School, Boston, MA 02115, USA

[3]Division of Digestive and Liver Diseases, Department of Medicine and Irving Cancer Research Center, Columbia University Medical Center, New York, NY 10032, USA

[4]Institute for Human Genetics and Department of Pediatrics, University of California, San Francisco, CA 94158, USA

[5]Department of Obstetrics, Gynecology and Reproductive Science and Eli and Edythe Broad Center for Regeneration Medicine and Stem Cell Research, University of California, San Francisco, CA 94143, USA

[6]Harvard Stem Cell Institute, Cambridge, MA 02138, USA

SUMMARY

Signals from the surrounding niche drive proliferation and suppress differentiation of intestinal stem cells (ISCs) at the bottom of intestinal crypts. Among sub-epithelial support cells, deep sub-cryptal CD81^{+} PDGFRA^{lo} trophocytes capably sustain ISC functions *ex vivo*. Here we show that mRNA and chromatin profiles of abundant CD81^{−} PDGFRA^{lo} mouse stromal cells resemble those of trophocytes and that both populations provide crucial canonical Wnt ligands. Mesenchymal expression of key ISC-supportive factors extends along a spatial and molecular continuum from trophocytes into peri-cryptal CD81^{−} CD55^{hi} cells, which mimic trophocyte activity in organoid co-cultures. Graded expression of essential niche factors is not cell-autonomous but dictated by the distance from bone morphogenetic protein (BMP)-secreting PDGFRA[hi] myofibroblast

[*]Corresponding author and Lead Contact: Ramesh A. Shivdasani, MD, PhD, Dana-Farber Cancer Institute, 450 Brookline Avenue, Boston, MA 02215, USA, ramesh_shivdasani@dfci.harvard.edu.

[#]These authors contributed equally.

aggregates. BMP signaling inhibits ISC-trophic genes in PDGFRA^{lo} cells near high crypt tiers; that suppression is relieved in stromal cells near and below the crypt base, including trophocytes. Cell distances thus underlie a self-organized and polar ISC niche.

eTOC

Shivdasani et al assign niche functions to specific mesenchymal cell types near stem cells at the base of intestinal crypts. They identify PDGFRA[lo] fibroblasts as a substantial source of requisite Wnt ligands and show that BMP signaling from crypt tops organizes functional heterogeneity of mesenchyme along the crypt vertical axis.

Graphical Abstract
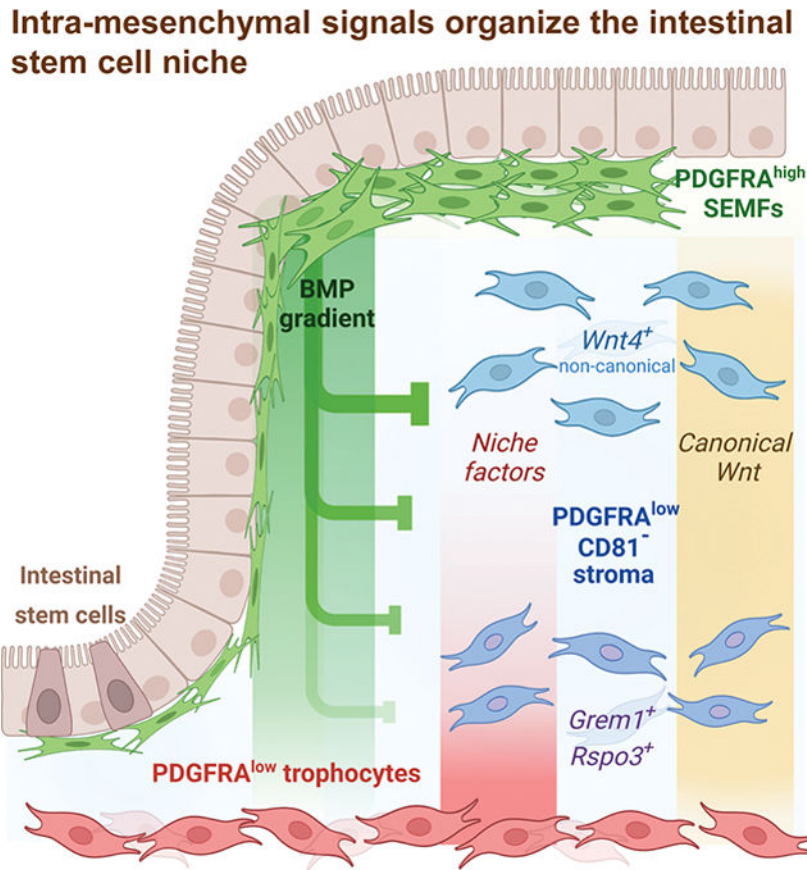
Keywords

Mesenchymal niche compartments; intestinal crypt structure and function; colonic crypts; intestinal Wnt source

INTRODUCTION

Lgr5[+] intestinal stem cells (ISCs) self-renew at the bottom of intestinal crypts, while their progeny proliferate and differentiate in higher crypt tiers;[1,2] epithelial 3D organoids replicate

these polar functions. Canonical Wnt signaling and bone morphogenetic protein inhibitors (BMPi) underlie intestinal tumors,[3] reinforcing the dependence of proliferating cells on canonical Wnt/R-spondin (Rspo) signaling and BMPi (Refs. [4–6]). However, the extent and determinants of crypt polarity are incompletely understood. Epithelial Paneth cells, which lie near ISCs, express canonical *Wnt3* (Ref. [7]) but ISCs are intact in the absence of Paneth cells[8,9] and the sub-epithelial mesenchyme likely dominates in sustaining ISCs and crypt polarity.[10]

Small intestine (SI) mesenchyme, once regarded as a loose collection of "myofibroblasts,"[11,12] is an organized tissue with distinct cell types that express multiple Wnt/Rspo and BMP agonists and antagonists.[13–18] *Foxl1*^{+} *Pdgfra*[hi] sub-epithelial myofibroblasts (SEMFs, also called telocytes) envelop all crypts and villi. SEMFs are proposed as a crucial Wnt source,[19,20] but they concentrate near SI crypt tops, express abundant BMPs and only non-canonical Wnts, and fail to support ISCs in culture.[17] In contrast, *Pdgfra*^{lo} CD34^{+} stromal cells support ISCs *in vitro*.[13–15,21] One spatially segregated subpopulation, sub-cryptal CD81^{+} trophocytes that express *Rspo3* and the BMPi *Grem1*, uniquely expands ISCs in the absence of exogenous factors.[22] SEMFs and trophocytes hence provide opposing cues for ISC self-renewal at the bottom and BMP-mediated epithelial differentiation at the top of SI crypts (Figure 1A).

In this model, *Pdgfra*^{lo} cells other than trophocytes appear possibly inert because they support organoid growth far less robustly.[17] However, the stromal CD81^{−} fraction outnumbers CD81^{+} trophocytes and together the two cell types are the major source of canonical Wnt ligands. Here we report that both *Pdgfra*^{lo} subpopulations harbor supportive activity in the SI and colon, together constituting a finely graded and self-organized niche. Spatial and molecular distinction of *Cd81*^{−} *Pdgfra*^{lo} cells, coupled with reliable *ex vivo* assays for ISC support, reveal this activity to include both functional Wnt signaling and extension of ISC-sustaining signals beyond trophocytes, into the immediate ISC vicinity. Intra-mesenchymal BMP signaling is prominent among a likely range of cues to generate diversity among *Pdgfra*^{lo} cells, driving functional polarity of the peri-cryptal ISC niche.

RESULTS

Distinction and fundamental similarity of intestinal Pdgfra[lo] subpopulations

Across independent studies,[17,23] three cell populations dominate in the mouse SI mesenchyme (Figure 1A): BMP-secreting PDGFRA[hi] SEMFs embedded in the basement membrane; abundant scattered sub-epithelial PDGFRA^{lo} cells of unknown function; and PDGFRA[lo] trophocytes, which lie beneath the muscularis mucosae and express *Ackr4* (Ref. [24]), CD81, BMPi, and RSPOs.[17,22] GFP^{+} cells in the adult *Pdgfra*[eGFP] mouse colon are similarly distributed.[25] GFP[hi] (PDGFRA[hi]) SEMFs envelop each crypt (Figure 1B–C), GFP[lo] *Ackr4*^{+} trophocytes localize under the muscularis mucosae, and additional GFP^{lo} *Ackr4*^{−} cells are present throughout the stroma (Figure 1C–D), interspersed between *Myh11*^{+} lamina propria myocytes and CD31^{+} blood vessels (Figure S1A). Beyond these anatomic features shared with the SI, graph-based cell clustering[26] of single-cell (sc) RNA-seq data from colonic CD45^{−} EPCAM^{−} mesenchyme (anchored by known molecular markers – Figure S1B) revealed identical population structures in the colon and SI, with

CD81$^-$ PDGFRA^{lo} stromal cells abundant in both organs (Figures 1E and S1C). Because scRNA data might conceal regional differences, we profiled mRNAs in purified bulk GFP$^+$ cell fractions from adult *Pdgfra^{eGFP}* mouse colon and distinct SI segments. Dividing the SI into 5 equal parts, we regard the first 1/5 as duodenum, the 3rd of 5 pieces as jejunum, the most distal 1/5 as ileum, and ~3 cm distal to the cecum as ascending colon (Figure 1F). As with their SI counterparts, flow cytometry readily separated colonic CD81$^+$ trophocytes from SEMFs and other PDGFRA^{lo} (GFP^{lo}) cells (Figure S1D). Overall, flow cytometry for Pdgfra$^+$ (GFP$^+$) cells in this study yielded ~23% GFP^{hi} SEMFs and ~77% GFP^{lo} cells in both SI and colon (Figure S1E). Bulk RNA-seq data from duplicate samples isolated from each intestinal segment were highly concordant (Figure S1F), marker genes confirmed accurate cell purification (Figure S1G), and *Hox* gene expression varied along the rostro-caudal axis as expected (Figure S1H). Lower difference in *Cd81* mRNA levels between colonic and SI PDGFRA^{lo} cells did not compromise separation of colonic CD81$^-$ stromal cells from CD81$^+$ trophocytes by flow cytometry (Figure S1D).

Unsupervised hierarchical analysis of bulk transcriptomes first clustered SEMFs apart from PDGFRA^{lo} cells, irrespective of intestinal segment, followed by distinction of colonic from SI cell types (Figure 1F). SEMFs showed substantial segmental variation (P_{adj}<0.01, log$_2$ fold-difference >1.5), whereas PDGFRA^{lo} populations (CD81$^+$ or CD81$^-$) from different SI segments showed few differences (Figure 1F and Table S1). Moreover, although CD81$^+$ trophocytes are superior to CD81$^-$ PDGFRA^{lo} cells in supporting ISCs in organoid assays[22] and the two cell types cluster separately in scRNA analysis (Figure 1E), mRNA differences between them are small in any segment (Table S1). We verified this similarity using the assay for transposase-accessible chromatin (ATAC-seq), which distinguishes cell types accurately and identifies loci poised for transcription.[27,28] Among *cis*-regulatory elements accessible in purified SI mesenchymal cells, 77% of 13,749 promoters and 21% of 31,525 enhancers (−1 kb or 2 kb from transcription start sites) were open in all three PDGFRA$^+$ populations. At the remaining accessible sites, chromatin was differentially open or closed in SEMFs but at least 94% of enhancers open in trophocytes were also open in CD81$^-$ cells (Figures 1G and S2A). Chromatin was accessible at the same sites in both PDGFRA^{lo} cell fractions at loci where mRNA levels robustly distinguish the two, such as *Ackr4* and *Cd81*, and at loci expressed equally in both cell types, such as *Sfrp1* (Figure S2A–B). Thus, whereas PDGFRA^{hi} and PDGFRA^{lo} cells differ in several ways, including ISC support,[17] PDGFRA^{lo} subsets are similar and key genes that distinguish the two PDGFRA^{lo} cell fractions may be controlled by extrinsic factors that operate differently above and below the muscularis mucosae.

CD81$^-$ PDGFRA^{lo} stromal cells are a key source of canonical Wnts

Among secreted factors implicated in ISC self-renewal, canonical Wnts are paramount[29,30] and ISCs depend critically on a mesenchymal source of ligands.[31] Two findings merit note. First, expression of Wnt-modulating genes varies across cell types and regions. *Wif1* is expressed only in SEMFs, while Wnt-sequestering factors expressed in PDGFRA^{lo} cells, such as *Sfrp1* and *Frzb*, decrease along the rostro-caudal axis. Other antagonists, such as *Dkk2* and *Apcdd1*,[32] are absent in the colon, while *Wls*, which is required for Wnt secretion[33,34] and expressed in all PDGFRA$^+$ cells, is highest in that segment (Figure S2C).

Although many factors determine tissue Wnt signaling, these mRNA findings point to a higher Wnt "tone" in the colon than in the SI. Second, among all 19 *Wnt* genes, bulk and scRNA-seq data identified only canonical *Wnt2*, *Wnt2b* and *Wnt9a* and non-canonical *Wnt*4, *Wnt5a* and *Wnt5b* in any PDGFRA$^+$ cell type (Figures S2D–E). *Wnt2* is expressed mainly in SI lymphatic vessels[35–37] and at low levels in colonic PDGFRA^{lo} cells (Figure S2D). The most prevalent canonical ligand, *Wnt2b*, is 10–15 times more abundant in PDGFRA^{lo} cells in all intestinal segments than in SEMFs, and its locus is accessible in PDGFRA^{lo} cells but not in SEMFs; conversely, the most prevalent non-canonical ligand, *Wnt5a*, is 8–9 times more abundant in SEMFs (Figures S2D and S3A). This distribution of Wnt ligand transcripts contradicts the view that SEMFs are a critical source of canonical Wnt ligands.[19]

That view rests in part on the finding that disruption of *Porcn*, a gene required for secretion of all Wnts,[38] in SEMFs triggered ISC and crypt failure.[19] As Cre recombinase activity in the study was driven by an ostensibly SEMF-specific *Foxl1* transgene that is vulnerable to silencing, the authors generated mice with a tandem *Cre-tdTomato* cassette knocked in to the *Foxl1* locus and found tdTomato principally in villus tip SEMFs.[39] Our examination of *Foxl1*$^{Cre-tdTomato}$ mouse colon also revealed tdTomato only in SEMFs at crypt apices, with rare recombination of the reporter gene *Rosa26*^{YFP} (Figure S3B); flow cytometry identified ~1% tdTomato$^+$ cells (Figure S3C). We therefore evaluated *Pdgfra*^{CreERT2} mice,[40] crossing them first with *Rosa26*$^{mG/mT}$ reporter mice[41] so that tamoxifen would convert baseline red membrane fluorescence in all cells into membrane GFP in Cre$^+$ cells (Figure S3D). Flow cytometry revealed GFP in 13% of mesenchymal cells, about half of which (6%) expressed CD34, a marker specific to *Pdgfra*^{lo} cells, and the other half represented CD34$^-$ SEMFs (Figure S3E, see also Figures S1B and S1G). Based on cell fractions in CD34 flow cytometry of *Pdgfra*^{H2BeGFP} mesenchyme (Figure S3E), we conclude that *Pdgfra*^{CreERT2} marks the majority of SEMFs and a considerably smaller fraction of *Pdgfra*^{lo} cells. Indeed, tamoxifen elicited robust GFP signals in SI and colonic SEMFs, notably including those at the crypt base; scattered *Pdgfra*^{lo} cells also turned green, but the majority did not (Figures 2A and S3D). Ten days after the last of 5 daily injections of tamoxifen, *Pdgfra*^{CreERT2} mice crossed with the *Porcn*^{Fl} strain[42] (*Porcn*-null) showed *Porcn* gene disruption in cells isolated by PDGFRA$^+$ flow cytometry, but no overt intestinal histopathology or defects in crypt cell replication and expression of ISC or Wnt target genes (Figures 2B–C and S3F). Although a small fraction of SEMFs may have evaded *Porcn* deletion, these findings coupled with their negligible levels of canonical Wnt transcripts argue against SEMFs as a critical Wnt source. Conversely, intestinal PDGFRA^{lo} cells express canonical Wnts and largely resist perturbation in *Pdgfra*^{CreERT2} mice, suggesting that they are the predominant source.

We used Wnt-dependent functional assays to test this possibility *in vitro*. *Wnt3*$^+$ Paneth cells, which lie near ISCs *in vivo*, enable organoid growth from SI crypts or isolated ISC-Paneth doublets in the absence of supplemental Wnt.[7] In contrast, organoid growth from *Atoh1*-null crypts, which lack Paneth cells,[8,43,44] or from colonic crypts requires exogenous Wnt[9] or pharmacologic activation of the Wnt pathway with, for example, glycogen synthase kinase 3 inhibitor CHIR99021 (CHIR). Indeed, Paneth cell-depleted crypts isolated from *Vil1-Cre*^{ERT2};*Atoh1*$^{fl/fl}$ mice (*Atoh1*-null, Figure S4A) and cultured in EGF, Noggin, and RSPO1 (ENR medium)[4] required CHIR to spawn organoids (Figure

2D). Substituting CHIR with purified SI or colonic CD81⁻ stromal cells or trophocytes potently rescued organoid formation in ENR medium, while SEMFs from either location did not (Figures 2E and S4B). To confirm that this PDGFRA[lo] cell effect reflects Wnt secretion, we added Wnt-C59, a PORCN inhibitor that blocks Wnt secretion.[45] Wnt-C59 abrogated organoid formation (Figures 2E and S4B) and this effect did not represent generic toxicity because the compound did not affect organoids formed in the presence of CHIR (Fig. S4C). SI and colonic PDGFRA^{lo} cells, but not SEMFs, also enabled Wnt-dependent organoid growth from wild-type colonic crypts (Figure 2F–G), similar to CHIR (Figure S4D). Mesenchymal cells retained pertinent transcripts during their brief *in vitro* expansion before crypt co-culture (Figure S4E) and they remained viable, with intact GFP (PDGFRA) expression, during co-culture (Figure 2F). Thus, both CD81⁻ and CD81⁺ PDGFRA^{lo} cells are *bona fide* sources of canonical Wnt. Of note, and in line with a previous report,[46] *Wnt2b* is expressed evenly over the length of colonic crypts and SI crypt-villus units (Figures. 2H and S4F), paralleling the distribution of PDGFRA^{lo} cells.

Molecular heterogeneity of CD81⁻ PDGFRA^{lo} stroma

Although *Wnt2b* is expressed equally in both PDGFRA^{lo} populations, canonical Wnt signaling would concentrate near ISCs because limiting RSPO co-factors[47] are abundant in trophocytes[17,22] (Figure 3A). Potent ISC-directed activity of the latter cells is attributed to expression of both *Rspo3* and *Grem1*,[17,22] which are highest in bulk trophocytes from all intestinal segments, but also expressed at lower levels in CD81⁻ stromal cells (Figures 3B and S5A). Moreover, in situ hybridization (ISH) signals for both factors extend above the muscularis mucosae, into *Ackr4*⁻ stromal cells (Figure 3B), suggesting that cells other than trophocytes may also harbor niche activity.

In scRNA-seq data from whole colonic mesenchyme, *Rspo3* and *Grem1* mapped principally to CD81⁺ trophocytes, but also to a CD81⁻ PDGFRA^{lo} cell subset, distinct from a complementary subset expressing non-canonical *Wnt4* (Figure 3C). Indeed, a pseudotime algorithm[48] that ranked all PDGFRA^{lo} cells according to their transcriptional similarity to trophocytes revealed gradients of decreasing *Grem1* and *Rspo3* and increasing *Wnt4* expression (Figure 3C), hence identifying useful proxies for seemingly distinct PDGFRA^{lo} cell states. To confirm this duality, we purified 2,040 additional CD81⁻ PDGFRA^{lo} colonic cells by flow cytometry. Aggregate scRNA analysis of all CD81⁻ PDGFRA^{lo} cells from bulk mesenchyme (Figure 1E) and this additional isolation of CD81⁻ stroma verified non-overlapping expression of *Grem1* and *Rspo3* in one subpopulation and *Wnt4* in the other (Figure 3D). This mRNA reciprocity was also evident in independent data[23,49] from adult mouse SI and colonic mesenchymal cells (Figure S5B).

To determine if these select gene markers reflect distinct cell states, we examined differential gene expression without marker supervision and independent of graph-based cell clustering. In scRNA data from colonic (this study) or SI (Ref. [17]) mesenchyme, consensus non-negative matrix factorization (cNMF)[50] identified distinct gene co-expression programs (GEPs) in various cell populations (Figure S5C and Table S2). Projecting these GEP modules onto UMAP plots revealed the expressing populations, e.g., SEMFs, myocytes and endothelial cells, each displaying unique GEPs (Figure S5D). Although modules 17 (SI)

and 6 (colon), which contain *Grem1* and *Rspo3* among the top-weighted genes, mapped predominantly to trophocytes, expression stretched into a fraction of CD81$^-$ PDGFRA^{lo} cells; conversely, GEPs 15 (SI) and 3 (colon), which contain *Wnt4* and other genes, projected onto a distinct, non-overlapping subset of CD81$^-$ stroma (Figure 3E).

To further confirm stromal heterogeneity, we fractionated wild-type SI mesenchyme by flow cytometry with PDGFRA antibody. Among the 3,370 cells recovered for scRNA analysis, both a marker-based supervised analysis and cNMF identified *Grem1*, *Rspo3*, and the corresponding GEPs extending from trophocytes into the CD81$^-$ stroma, with *Wnt4* expressed in a different *Cd81*$^-$ cell fraction (Figure 3F). As expected from scRNA data (Figure S2D–E), *Wnt4* is also present in SEMFs. cNMF identified the respective *Grem1*$^+$ or *Wnt4*$^+$ modules across independent datasets of whole mesenchyme from SI (Ref. [17]), colon, and SI PDGFRA$^+$ cells, with large overlap among the top 100 genes (Figure S5E). Across PDGFRA^{lo} cells ranked by overall transcriptional similarity (diffusion pseudotime method[51]), the *Grem1*$^+$ and *Wnt4*$^+$ modules were expressed reciprocally (Figure 3F). Importantly, genes in the respective modules, such as *Aebp1, Cxcl14, and Lpl,* are distributed variably across *Cd81*$^-$ cells (Figure S5F) and the *Grem1/Rspo3*$^+$ fraction is not a trophocyte replica: ISC-trophic mRNA levels are lower than in trophocytes (Figure 3B), where transcripts such as *Ackr4* are highly restricted.

Spatial and functional heterogeneity of CD81$^-$ PDGFRA^{lo} stroma

ISH signals for *Rspo3* were limited (Figure 3B) by low mRNA levels and probe efficiency, but *Grem1* signals were consistent and showed asymmetric distribution. In both SI and colon, *Grem1*$^+$ cells above the muscularis were restricted to the lower crypt and excluded from villi or upper crypt regions, while *Wnt4* was reciprocally expressed in *Grem1*$^-$ cells located high in crypts and in SI villus stroma (Figures 4A and S6A). We verified this asymmetry in two independent mouse models. First, we crossed *Wnt4*$^{eGFP-CreERT2}$ knock-in mice[52] with the *Rosa26*$^{LSL-TdTom}$ strain[53], hence marking *Wnt4*$^+$ cells with fluorescence; RT-PCR analysis of FACS-purified tdTom$^+$ cells confirmed that they represent the *Wnt4*$^+$ fraction (Figure S6B). tdTom$^+$ cells included SEMFs, as expected from scRNA data (see Figure S2E), as well as stromal cells in the lamina propria, with a firm boundary in upper crypt regions (Figures 4B and S6C). Along the radial axis, these *Wnt4*$^+$ stromal cells lie farther from the epithelium than SEMFs and, distinct from SEMFs, they co-express *Sfrp1* and stain poorly with PDGFRA antibody (Ab, Figure S6C). Second, we generated a *Grem1* reporter allele with in-frame insertion of a *DTR-tdTomato* cassette, which places fluorescence in *Grem1*-expressing cells (Experimental Methods). Smooth muscle cells showed bright tdTom signals, as expected; additional non-muscle *Grem1*$^+$ cells were confined to a few peri-cryptal mesenchymal tiers above the muscularis (Figure 4C). Thus, trophic factor expression extends beyond sub-muscularis trophocytes, into PDGFRA^{lo} cells that concentrate near the crypt base, distinct from *Wnt4*$^+$ cells in higher mesenchymal tiers (Figure 4D).

This mesenchymal polarity suggests that the *Grem1*$^+$ *Rspo3*$^+$ subset may provide the limited organoid support from unfractionated CD81$^-$ PDGFRA^{lo} cells and we therefore sought to separate them from the putative inactive (*Wnt4*$^+$) fraction. Projection of differentially

expressed genes in colonic GEP module 6 (which contains *Grem1* and *Rspo3* – Table S2) revealed higher *Cd55* mRNA levels in the corresponding CD81^{−} stromal cell fraction (Figure 5A). *Cd55* encodes a cell surface protein, is also represented in SI GEP module 17 (though not among the 100 top-weighted genes), and was recently reported to predominate in colonic *Grem1*^{+} cells near the crypt base.[54] Indeed, our separation of CD55^{lo} from CD55^{hi} cells by flow cytometry revealed asymmetric *Wnt4* and *Grem1/Rspo3* expression (Figure 5B). Testing these mesenchymal fractions for differential niche activity required a sensitive *in vitro* assay, and because colonic crypts form small organoids in variable numbers and require large number of mesenchymal cells, which hampers organoid quantitation. We therefore co-cultured duodenal crypts with colonic or duodenal CD55^{lo} or CD55^{hi} cells. The latter cells consistently spawned larger organoids in substantially larger numbers (Figure 5C). Thus, the CD55^{hi} subset of CD81^{−} stromal cells provides demonstrable niche support; when crypts are cultured with unfractionated PDGFRA^{lo} cells, the complementary *Wnt4*^{+} cell fraction likely masks this activity.

BMP-mediated self-organization underlies ISC niche polarity

These findings together suggest that local cues might influence the niche potential of sub-cryptal CD81^{+} trophocytes and peri-cryptal CD81^{−} CD55^{hi} cells; specifically, that these PDGFRA^{lo} cells may realize latent niche potential as a function of their locations. As all functional data point to similar PDGFRA[lo] cell activity in the SI and colon, putative inductive signals must be present in both organs. Thus, although lymphatic vessels are implicated in ISC support,[35] they are poor candidates for *niche organization* because lacteals are only present in SI lamina propria and large sub-mucosal lymphatic vessels are irregularly spaced, so many crypts lie far from them (Figure S7A). In contrast, PDGFRA[hi] SEMFs are uniformly present in the SI and colon, aggregating densely at two SI sites: villus tips and bases.[17] Similarly, colonic SEMFs are abundant under the luminal epithelial cuff and consistently less dense below that region, as seen both in *Pdgfra*[eGFP] colon (Figure 6A) and in wild-type mice using PDGFRA Ab (Figure S7B). These cells are the predominant BMP source in both SI and colon (Figure S7C – PDGFRA^{lo} cells express low levels, especially *Bmp4*) and, in line with that observation, colonic ISH signals for *Bmp4* and *Bmp5* concentrate at sub-luminal SEMF aggregates (Figure 6B). Furthermore, the BMP-responsive gene *Id1* is expressed at higher levels in functionally inert CD81^{−} CD55^{lo} stromal cells compared to CD55^{hi} cells, similar to *Wnt4* (Figure 5B). SEMF-derived BMPs are thus candidate self-organizing signals for the ISC niche.

Crypts are nearly twice as long in the adult rat and weanling mouse colon than in the SI (Refs. [55,56]). We confirmed that the significant difference in crypt height persists in adult mice (Figures 6C and S7D). Therefore, ISCs in the colonic crypt base and the colonic niche are farther from SEMF-derived products than their SI counterparts, so if SEMF-derived BMPs organize the niche, then colonic SEMFs must produce larger amounts than those in the SI. *Bmp2* and *Bmp5* levels are indeed highest in colonic SEMFs, while levels of the BMPi *Chrd* are lowest (Figure 6D and Table S1 – *Bmp4* levels in PDGFRA^{lo} cells, albeit lower than BMP gene levels in SEMFs, are also highest in the colon). Moreover, both trophocytes and CD81^{−} PDGFRA^{lo} stromal cells express abundant *Bmpr1a* and *Bmpr2* receptor transcripts and have accessible chromatin at key BMP-responsive *Id1-3* loci (Figure

6E), consistent with their potential to react to BMP signaling. Together, these findings support the idea that SEMF-derived BMPs inhibit PDGFRA^{lo} cell expression of ISC niche genes, such as BMPi, hence positioning functional niche cells at set distances from the BMP source (Figure 6F). In this model, PDGFRA^{lo} cell heterogeneity is not cell-intrinsic but locally determined, and the requisite epigenetic plasticity is reflected in near-identical configurations of open chromatin at niche-relevant loci, such as *Grem1*, *Rspo3*, and *Cd55* (Figure 6G).

To test this model, first we treated primary intestinal CD81$^-$ CD55^{hi} PDGFRA^{lo} cells in culture with mixtures of recombinant (r) BMPs (rBMP2/4/7) or BMPi (rGREM1, rNOG). Elevated phosphor-SMAD1/5 levels (pSMAD, Figure 7A) and nuclear pSMAD immunofluorescence (Figure 7B), confirmed BMP signaling *in vitro*. In response to this stimulation of SI and colonic stromal cells, *Wnt4* mRNA, which marks PDGFRA^{lo} cells closest to SEMF aggregates (and farthest from ISCs) *in vivo*, increased 16-fold on average compared to untreated controls, whereas *Rspo3*, *Grem1* and *Cd55*, which mark PDGFRA^{lo} cells near the crypt base and farthest from SEMF aggregates *in vivo*, consistently declined 1.5- to 8-fold (Figure 7C). Of note, rBMP exposure markedly reduced endogenous *Bmp4* expression and, as a sign of specificity, other genes such as the EGF ligands *Ereg* or *Nrg1* were unaffected. Conversely, treatment with rBMPi increased expression of *Bmp4* and *Cd55*; because BMPi effects *in vitro* rely on *inhibition* of likely weak native BMP signals, they were predictably less potent (Figure 7C). Trophocytes reacted similarly to rBMP exposure, with notable induction of *Wnt4* and suppression of niche-relevant factors, including trophocyte-specific marker *Cd81* (Figure 7D). To assess the functional consequences of these effects, we introduced rBMP-treated CD81$^-$ CD55^{hi} PDGFRA^{lo} cells into crypt co-cultures, anticipating that prolonged withdrawal of BMP might attenuate the phenotype. Nevertheless, treated cells in each experiment yielded smaller organoids than untreated cells (Figures 7E and S7E).

If SEMF-derived BMP signaling indeed influence phenotypes of other sub-epithelial cells, then nuclear pSMAD should localize in roughly the same tiers in the mesenchyme as in BMP-responsive epithelium. Thus, *Wnt4*$^+$ stroma should express pSMAD and localize in close alignment with epithelial pSMAD$^+$ cells, which extend from villus base to tip in the SI and across the top half of colonic crypts. Immunostaining of *Wnt4^{CreERT2};R26R^{tdTom}* mouse intestines revealed exactly this pattern: both *Wnt4*$^+$ stromal cells and adjoining epithelial cells showed nuclear pSMAD, while both epithelial and stromal cells in lower tiers lacked pSMAD (Figure 7F). Together, these findings implicate BMP signaling in regulation of niche factor genes in PDGFRA^{lo} cells. They suggest that the position of ISC-supporting mesenchymal cells near the crypt base is determined, at least in part, by their distance from supra-cryptal SEMF aggregates, which provide BMP agonists, and their proximity to various sub-cryptal sources of BMPi (Figure 7G).

DISCUSSION

Countervailing Wnt and BMP gradients underlie intestinal crypt homeostasis. ISCs require high Wnt/Rspo and absent BMP activity,[57–60] and sub-epithelial mesenchyme is the predominant source of Wnt/Rspo and BMP ligands and inhibitors.[10,13–15,17,18,61, 63] Signal

gradients could arise because key mesenchymal cells occupy opposite sides of the crypt base or because cells express agonists and antagonists in a graded fashion; recent investigation of the intestinal mesenchyme has brought these possibilities into focus.[15–17,19,20,61–63] PDGFRA^{lo} CD81^{+} *Ackr4*^{+} trophocytes lie beneath the muscularis mucosae, express *Grem1* and *Rspo3*, and robustly support organoid growth from isolated crypts.[17] Conversely, SEMFs concentrate near crypt tops and the BMP gradient is thought to reflect opposing foci of agonist-secreting SEMFs at crypt tops and antagonist-secreting trophocytes near the crypt base.[17] Another mesenchymal population of PDGFRA^{lo} CD81^{−} *Ackr4*^{−} cells is abundant, but because these cells populate the whole crypt-villus axis, express little BMPi or RSPO, and support ISCs poorly *ex vivo*, their contribution to the ISC niche previously seemed insignificant.[17] Previous identification of PDGFRA[lo] cell population substructure by scRNA-seq[25,49] also appears unrelated to known niche properties, e.g., extracellular matrix.[54] We show here that CD81^{−} PDGFRA^{lo} cells located above the muscularis mucosae are a potent source of canonical Wnt and that a CD55^{hi} fraction bathing crypt bottoms expresses key niche factors and promotes organoid growth *ex vivo*. The roles of molecular markers such as CD81 and ACKR4 remain unknown and CD81 expression in various PDGFRA^{−} mesenchymal cells limits its utility to isolating trophocytes from other PDGFRA^{+} cells (see Figures S1 and S4).

Our study highlights four salient features of the ISC niche: extension beyond sub-mucosal trophocytes, into a defined peri-cryptal domain; functional cellular heterogeneity along the crypt vertical axis; overlapping, graded sources of diffusible supportive factors; and, most notably, self-organization. The findings deliver a coherent picture in which SI and colonic ISCs draw support, including canonical Wnts, from transcriptionally, anatomically, and functionally distinct CD81^{+} (trophocyte) and CD81^{−} pools of PDGFRA^{lo} cells. Ablation of leptin-receptor *(Lepr)*-expressing cells, which fortuitously encompass *Grem1*^{+} PDGFRA^{lo} cells, was recently reported to reduce ISC numbers, distort crypts, and impair their regeneration after γ-irradiation;[21] our findings are consistent with these observations. Goto *et al.* also found recently that cells expressing *Rspo3* and *Grem1* include trophocytes as well as CD81^{−} stromal cells,[36] and other spatial analyses have identified asymmetric distribution of selected mRNAs along the crypt axis.[35,64,65]

Nearly identical configurations of chromatin in CD81^{+} (trophocyte) and CD81^{−} PDGFRA^{lo} cells imply that their differences are not intrinsic and likely imparted by local determinants of niche self-organization. Our findings nominate SEMF-derived BMPs as a principal stimulus for the distinction between stromal cells that provide or do not provide key niche factors. Exposure to BMPs reduces *Grem1* and *Rspo3* mRNA levels in PDGFRA^{lo} cells; these factors are accordingly expressed as a function of the cells' distance from crypt tops, where SEMFs aggregate. We therefore propose that SEMFs provide BMPs not only as a cue for epithelial cells to mature near crypt tops[66] but also to inhibit niche activity in neighboring mesenchymal cells. Circumstantial (Figure 6) and experimental (Figure 7) evidence support a model in which BMPs repress niche genes at the tops of crypts. Increasing distance from this concentrated BMP source, likely coupled with proximity to sources of BMPi, relieves that repression modestly in CD81^{−} stroma near the crypt base and robustly in CD81^{+} trophocytes, the PDGFRA^{lo} cells that lie farthest from SEMF aggregates (Figure 7G). Whereas colonic SEMFs aggregate only at crypt tops, those in the

SI additionally aggregate at the tops of villi.[17] This additional BMP reserve in the SI can explain why *Wnt4*+ cells, i.e., those subject to BMP-mediated repression of niche factors, are not confined to the tops of crypts but extend throughout the villus lamina propria.

Beyond this proposed simple mechanism for mesenchymal self-organization, other signals likely help craft a complex ISC niche. *Wnt4*+ stromal cells, for example, are well positioned to provide factors that also suppress niche activity at crypt tops and in villi; *Wnt4* is a transcriptional target of BMP signaling in PDGFRA^{lo} stromal cells and it or other genes might help restrict niche size and ISC location. Conversely, although BMPi do not activate niche factor genes *in vitro* as potently as BMPs repress them (Figure 7C), that finding may reflect absence of supplemental BMP and other, unknown variables in primary cell cultures; *in vivo*, various sub-cryptal sources of BMPi, such as trophocytes and smooth muscle, may enhance niche activity of PDGFRA^{lo} stroma. Furthermore, while our studies focus on mRNA levels of genes known to support ISCs – not only *Grem1* and *Rspo3* but also ligands and modulators of canonical Wnt signaling– post-transcriptional and post-translational effects in each signaling pathway likely refine the milieu further for optimal ISC support. Finally, mesenchymal cell support of organoid growth in Matrigel droplets belies their layered arrangement *in vivo*. Note that crypts cultured with mesenchymal cells form spheroids and not budding organoids (e.g., Figures 5C and 7E); moreover, overt polarity of organoids cultured in soluble niche factors[4] implies that crypt epithelium itself harbors some degree of self-organization, a property that may well contribute to mesenchymal cell heterogeneity. For example, epithelial Hedgehog signals to mesenchymal and smooth muscle cells[67] might influence niche properties. Limited recovery of mesenchymal cells after crypt co-culture precluded critical assessment of their response to epithelial cell exposure.

From imaging studies in reporter mice (Fig. 4), the boundary between non-overlapping *Wnt4*+ and *Grem1/Rspo3*+ subpopulations of peri-cryptal PDGFRA^{lo} cells appears to lie near the crypt equator. As both ISH and reporter gene activity have limits in sensitivity, we cannot exclude low expression of genes from each cell population in the other. The scRNA expression domain of *Cd55*, a target of BMP repression similar to *Grem1* and *Rspo3*, accentuates this point because it tracks expression of the latter genes imprecisely (Figure 5A). Nevertheless, CD55 flow cytometry is effective at separating the active *Grem1*+ *Rspo3*+ fraction of CD81− stromal cells from the inert *Wnt4*+ fraction. Thus, although the significance of *Cd55* and non-canonical *Wnt4* expression in distinct PDGFRA^{lo} stromal cells is unknown, they are useful molecular markers of cells that support (*Cd55*) or do not support (*Wnt4*) ISC functions.

Limitations of the study

Genetic ablation of discrete cell populations or depletion of candidate genes from those cells could help refine emerging models of the ISC niche, but neither approach is currently practical because candidate niche factors are generally redundant with each other, and molecular markers are not strictly restricted to single cell types. For example, *Cd81* and *Ackr4* accurately distinguish trophocytes from other PDGFRA^{lo} cells, and *Cd55* levels separate active from inactive PDGFRA^{lo} stromal cells, but expression of these markers

outside the PDGFRA^{lo} compartment limits experimental possibilities and interpretations. Moreover, intestinal mesenchymal cells expel tamoxifen, a conventional agent to activate Cre recombinase.[68] We overcome this limitation in part using organoid assays, which reveal crucial differences, for example between PDGFRA^{lo} cells and SEMFs as Wnt sources and between CD55^{hi} and CD55^{lo} cells in ISC support; however, *ex vivo* interrogation of niche functions lacks the context of *in vivo* cell interactions. Furthermore, although we handled diverse mesenchymal cells in parallel for organoid assays and they retain the tested native transcripts *in vitro*, the degree of inevitable phenotypic drift in culture is unknown. Finally, our focus on BMP-mediated transcriptional control as an organizing principle for the ISC niche is necessarily reductionist. Other signaling pathways, epithelial-stromal interactions, and post-transcriptional effects must also contribute toward ISC support *in vivo*. Our delineation of BMP effects provides a foundation to investigate additional niche determinants, not only in the resting state we investigated in the current study but also in disease states.

STAR METHODS

RESOURCE AVAILABILITY

Lead contact—Further information and requests for resources and reagents should be directed to and will be fulfilled by the lead contact.

Materials availability—Materials used in this study are listed in the Key Resources Table.

Data and code availability—Sequencing data have been deposited in the Gene Expression Omnibus (GEO) repository under the accession numbers GSE211275 and GSE212601 as listed in the Key Resources Table. Data are publicly available as of the date of publication.

This study includes analysis of previously published data, referenced with the accession numbers in the Key Resources Table.

This study used custom functions in a Python environment (3.7.13) available at Zenodo, DOI:10.5281/zenodo.7686568

Any additional information required to reanalyze data reported in this paper is available from the lead contact upon request.

EXPERIMENTAL MODEL DETAILS

Mouse strains and husbandry—All animal procedures were approved by Animal Care and Use Committees at Dana-Farber Cancer Institute or Columbia University Medical Center. Mice were housed in 12-hour light/dark cycles with constant temperature and ad libitum access to food and water. Strains were maintained on a mixed C57BL/6 background and both male and female mice aged 8–16 weeks were used. *Pdgfra^{H2BeGFP}* (JAX strain 007669)[69], *Myh11^{CreERT2}* (JAX strain 019079)[70], *Atoh1$^{fl/fl}$* (JAX strain 008681)[44], *Wnt4^{CreERT2}* (JAX strain 032489)[52], *Rosa26$^{LSL-TdTomato}$* (JAX strain 007909)[53], *Pdgfra^{CreERT2}* (JAX strain 032770)40, *Rosa26$^{mT/mG}$* (JAX strain

007676)[41], $FoxL1^{CreERT2–2A\text{-}tdTomato}$ (RRID: MMRRC_068163-JAX)[39] and $Rosa26^{EYFP}$ (JAX strain 006148)[71] mice were purchased from the Jackson Laboratories. $Porcn^{fl/fl}$ mice[42] and $Vil1^{CreERT2}$ mice[72] were generous gifts from C. Murtaugh (University of Utah) and from S. Robine (Institut Curie, Paris), respectively. For Grem1-DTR^{tdTom} mice, a targeting vector pMCS-Grem1-P2A-DTR-P2A-TdTomato was created to replacing the translational stop codon TAA in the *Grem1* locus. Male chimeras were made by injecting correctly targeted FL19 (C57BL/6N) embryonic stem cells into C57BL/6J blastocysts.

Tamoxifen (Sigma, 1 mg) dissolved in sterile sunflower oil (Sigma) was injected intraperitoneally for 3 or 5 days (as specified) to induce cell-type-specific gene recombination via Cre^{ERT2}. Injected Cre-negative littermates were used as controls. $Vil1\text{-}Cre^{ERT2}$;Atoh1$^{fl/fl}$ (*Atoh1*-null) mice were sampled 3 weeks after the tamoxifen injection to ensure abolition of secretory cells, including long-lived Paneth cells. For imaging studies, $Pdgfra^{H2BeGFP}$;$Myh11^{CreERT2}$;$R26R^{LSL\text{-}TdTomato}$ mice were harvested 5 days after 2 daily tamoxifen injections. $Wnt4^{CreERT2}$;$Rosa26R^{LSL\text{-}TdTomato}$ mice were given tamoxifen, 6 mg dissolved in corn oil, by oral gavage on 3 consecutive days. $FoxL1^{CreERT2–2A\text{-}tdTomato}$;$Rosa26^{EYFP}$ mice used for whole-mount imaging and all $Pdgfra^{CreERT2}$ mice were injected on 5 consecutive days with 1 mg tamoxifen daily. $Pdgfra^{CreERT2}$;$Porcn^{fl/fl}$ (*Porcn*-null) female mice were injected for 5 consecutive days with 1 mg tamoxifen daily and examined 10 days later. Injected Cre-negative littermates served as controls.

METHOD DETAILS

Sampling and cell isolation—To sample distinct intestinal regions, we divided the small intestine (SI) from stomach end to ileocecal junction into 5 segments of equal length, designated the first segment as Duodenum, the third segment as Jejunum, and the fifth segment as Ileum; intermediate regions were discarded. The proximal half of colon (~3 cm) was also used. Littermates of $Pdgfra^{H2BeGFP}$ mice lacking this *Gfp* allele were used to isolate intestinal crypts.

Mesenchymal cell isolation—Mesenchymal cells were isolated as described previously[17]. Briefly, mice were sacrificed and perfused with phosphate-buffered saline (PBS) by cardiac injection. Intestines were harvested, washed in PBS, and the outer muscle layer was removed with tweezers under stereomicroscope guidance. Tissue pieces were incubated twice, shaking at 300 rpm at 37°C for 15 min each time, in 10 mM EDTA in Hank's Balanced Salt Solution (HBSS, Wisent) +10 mM HEPES (Gibco) +5% fetal bovine serum (FBS, Sigma). Epithelium-depleted pieces were then washed in HBSS +10 mM HEPES and digested with 3 mg/ml Collagenase 2 (Worthington) for 20 min under rotation at 30 rpm at 37°C. The resulting cell suspension was filtered through a 40 μm mesh (Falcon), centrifuged at 300 *g* for 10 min at 4°C, and washed again in HBSS +10 mM HEPES before staining procedures and flow cytometry.

Unfractionated mesenchyme isolates for expansion culture were centrifuged at 300 *g* for 10 min at room temperature and kept in Advanced DMEM (Life Technologies) supplemented with 10% FBS (Sigma) for 3 days.

Flow cytometry for *Foxl1^tdTom^, Pdgfra^CreERT2^* and *Pdgfra^H2BeGFP^* was performed on cells stained for CD34 (Biolegend, 119310, 1:100) or PDGFRA (CD140a, BioLegend 135905, 1:100), as indicated, for 20 min at 4°C in FACS buffer (HBSS, 10 mM HEPES, 2 mM EDTA, 0.5% bovine serum albumin (Sigma)). Single cell (sc)RNA-seq of *Pdgfra^H2BeGFP^* cells proceeded on unstained cells sorted by GFP levels. For colonic whole mesenchyme scRNA-seq, cells were stained with EpCAM (eBioscience, 12-5791-83, 1:100) and CD45 (Invitrogen, 17045182, 1:100) antibodies (Ab) to exclude epithelial and immune cells.

For scRNA-seq of small intestinal PDGFRA$^+$ stromal cells, 10 cm of jejunum from a male 8-week-old mouse were dissected, flushed with cold PBS, and opened longitudinally. Tissue was cut into small pieces and incubated in cold PBS +10 mM EDTA to release epithelial cells and the remaining fragments were digested using Collagenase XI (Sigma) and Dispase II (Sigma) for 30 min at 37°C. Filtered single cells were stained with PDGFRA (Biolegend, 135905) and CD31− Ab for 20 min on ice and live (DAPI$^-$) CD31$^-$ PDGFRA$^+$ cells were isolated.

For all other experiments, cells were stained with biotinylated anti-CD81 (eBiosciences 13-0811-81, 1:50) or control biotinylated IgG for 25 min at 4°C in FACS buffer, washed, and incubated with streptavidin-APC (eBiosciences, 17431782, 1:100). For CD55 sorting, anti-CD55-PE (Biolegend, 131803, 1:100) or control IgG-PE (Biolegend, 400907, 1:100) Ab was added to streptavidin-APC during the second incubation. Each staining step was followed by centrifugation (300 *g*, 5 min, 4°C) and washing in FACS buffer.

Fluorescence-activated cell sorting—Mesenchymal cells were sorted using a BD FACS M Aria II instrument with 100 μm nozzle. Cells were collected in FACS buffer and used directly to extract RNA or washed with Dulbecco's Modified Eagle Medium (DMEM, Gibco) for organoid co-culture and sub-culture.

Bulk RNA-sequencing—Freshly sorted mesenchymal cells from different intestinal regions were used immediately for RNA extraction with RNAeasy Plus micro kit (Qiagen). RNA integrity and concentration were determined using Agilent Bioanalyzer High Sensitivity RNA 6000 pico kits (Agilent). For samples with RNA-integrity number (RIN) >8.5, libraries were constructed using SMART-Seq v4 Ultra Low Input RNA kits and sequenced on the Novaseq platform (Illumina).

Single-cell RNA sequencing—8,000 cells were loaded onto a 10X Chromium controller followed by the Single Cell 3′ V3.1 assay (10X Genomics PN-120237). Libraries were constructed according to the manufacturer's recommendations and sequenced on the NovaSeq platform (Illumina).

Assay for Transposase-Accessible Chromatin (ATAC-seq)—ATAC-seq was performed on 50,000 live cells, sorted for PDGFRA level and presence of CD81, using the "Omni-ATAC" protocol[73] and library preparation as described previously[74]. After quantification by Qubit dsDNA high-sensitivity assay (Life Technologies) and assessment of library quality using a High Sensitivity DNA Kit on a Bioanalyzer 2100 instrument (both

Agilent), residual primers were excluded using AMPure beads (Beckman Coulter). Libraries were sequenced on the NovaSeq platform (Illumina).

Mesenchymal cell culture—As freshly sorted SEMFs grow poorly in isolation, we obtained adequate numbers for Wnt experiments by first culturing whole unfractionated mesenchyme up to 3 days in Advanced DMEM/F12 with 10% FBS before sorting ("expanded"). Cells were washed in PBS, digested with 0.25% Trypsin-EDTA (Gibco) for 5 min at 37°C, neutralized with DMEM +10% FBS, and centrifuged at 300 g for 5 min at room temperature before staining for CD81 and sorting. Cells were plated immediately after sorting with *Atoh1*-null (or control) SI crypts or wild-type colonic crypts and cultured in ENR medium or RNA was extracted to assess potential transcriptional drift.

Freshly isolated PDGFRA^{lo} cells sorted for CD81 and CD55, as described above, were expanded *in vitro* for 2–7 days in MesenCult Expansion medium (Stem Cell Technologies). For primary cell treatments, serum-free Advanced/DMEM/F12 medium was supplemented with a mix of BMP-2 (Peprotech), BMP-4 (Peprotech) and BMP-7 (R&D Systems) or a mix of GREM1 (Thermo Fisher) and NOG (Peprotech) at 100 ng/ml each. Cells were treated for 5 days, with replacement of the medium every 2 days, before harvest for qRT-PCR analysis or further assays.

For subsequent co-culture, sorted and expanded mesenchymal cells were washed in PBS, digested with 0.25% Trypsin-EDTA for 5 min at 37°C, neutralized with Advanced DMEM/F12 medium (Gibco) containing 10% FBS and centrifuged at 300 g for 5 min. Cells were transferred to ice, counted with a hemocytometer and pelleted by centrifugation before adding to freshly isolated intestinal crypts mixed in Matrigel (Corning) droplets (1,000 mesenchymal cells per μl Matrigel (i.e. 10,000 cells per 10 μl Matrigel droplet) for SI crypts or 2,000 mesenchymal cells per μl Matrigel (i.e. 20,000 cells per 10 μl Matrigel droplet) for colonic crypts).

Crypt isolation and Intestinal organoid culture—Crypt epithelium from dissected intestines was enriched by 2 successive incubations for 15 min in 2 mM EDTA (SI) or for 45 min in 5 mM EDTA (colon) in HBSS at 4°C on a tube rotator at 30 rpm. Washed crypts were shaken 30 times manually and filtered through a 70 μm mesh (Falcon) to separate crypts from villi (SI only). Crypt suspensions were centrifuged at 80 g at 4°C for 8 min, washed in DMEM, and centrifuged again. Between 50 and 100 crypts were added to 10 μl or 20 μl Matrigel (Corning) droplets, respectively, and mixed with mesenchymal cells (when applicable) before culture in 24-well plates or chamber slides (Nunc) to facilitate imaging.

Standard organoid medium (ENR) as described previously[4,17] contained Advanced DMEM, 1% B27 (Gibco), 0.5% N2-supplement (Gibco), 125 mM N-Acetylcysteine (Sigma), 10% Rspo1-conditioned medium (Harvard Digestive Disease Center), 100 ng/ml rNOG (Peprotech), 100 ng/ml rEGF (Peprotech) and 10 μM Y-27632 (Sigma). Co-cultures with *Atoh1*-null crypts occurred in organoid medium lacking R-spondin, rEGF, and rNOG unless otherwise specified. The GSK3-inhibitor CHIR99021 (Sigma, 5 μM) served as a positive control for canonical Wnt-activation. Porcupine inhibitor Wnt-C59 (Thermo Fisher, 100

nM/ml) was added immediately after plating. Co-cultures were maintained at 37°C and 5% CO2 and the medium replaced every two days.

Brightfield images were acquired with a CKX53 microscope (Olympus) using 4X or 2X objectives to count structures. Organoids were counted manually across the entire well using Fiji (ImageJ 1.52p) software and the Multi-point tool to mark counted structures. Organoid diameters were measured by drawing mid-organoid lines that we quantified using the Measure tool in Fiji. Measurements were summarized in Excel (Microsoft) and plotted using Prism9 (Graph Pad).

RNA extraction, reverse transcription, and qRT-PCR—Freshly sorted cells were pellet and lysed in RLT Plus buffer (Qiagen). DNA elimination and RNA extraction were achieved using RNeasy Plus Micro kit (Qiagen).

Cultured cells or isolated crypts were lysed in TRIZOL reagent (Life Technologies) and RNA was extracted by combining TRIZOL-chloroform extraction with RNA-binding columns (PureLink kit). RNA (50–200 ng, quantified by NanoDrop spectrophotometer (Thermo Fisher) was reverse transcribed using SuperScript kit (Life Technologies) according to the manufacturer's instructions. Gene expression levels were measured by real-time PCR using Power SYBR reagents (Life Technologies) on a BioRad instrument.

Tissue processing and immunofluorescence—Mice were perfused with 4% paraformaldehyde and intestines were fixed overnight at 4 °C. After washing in PBS, samples were placed in sucrose gradients of 10% (6 h, 4°C), 20% overnight, and 30% overnight at 4°C. Tissue rolls were embedded in OCT medium (Sakura) and stored at −80°C until cryo-sectioning of 10 μm slices onto Superfrost Plus microscope slides (Thermo Fisher). Goblet cells were visualized using the Alcian Blue stain kit (H3501, Vector Laboratories) according to the manufacturer's recommendations. Paneth cells were visualized after blocking slides for 1 h with 5% goat serum in PBST followed by incubations with anti-LYZ Ab (Dako, A009, 1:100 dilution in blocking buffer) at 4°C overnight, AlexaFluor anti-rabbit secondary antibody (Life Technologies), and Vectashield+DAPI mounting medium (Vector Laboratories).

For hematoxylin and eosin (H&E) images, formaldehyde-fixed tissues were processed to paraffin-embedded (FFPE) blocks, followed by cutting 10 μm sections, H&E staining, and imaging (all performed by Servicebio).

For Phospho-SMAD and Ki67 staining, fixed frozen tissue sections (10 μm) were washed with PBS and antigens were retrieved by boiling for 1 min in 10 mM Citrate buffer (pH 6.0). Primary Pdgfra^{lo} CD81^{−} CD55^{hi} mesenchymal cells were cultured for 4 days in MesenCult on chamber slides and treated with rBMPs or rBMPi as above. Cells were fixed with 4% paraformaldehyde for 30 min at room temperature, permeabilized for 30 min with PBS +0.3% Triton-X100, and washed twice in PBS. Endogenous peroxidase activity in both tissue sections and fixed cells was blocked by incubation for 1 h with 0.3% H_2O_2 in TN buffer (0.1 M Tris-HCl, pH 7.5; 0.15 M NaCl). Slides were washed twice in TN buffer, blocked for 1 h at room temperature with 0.5% Blocking Reagent (Perkin

Elmer) in TN buffer +0.05% Tween-20 (BioRad), and incubated overnight with 1:300 dilution of anti-pSMAD1/5 (Cell Signaling Technologies, 9516) or anti-MKI67 (Invitrogen, MA5-14520) Ab at 4°C. Slides were washed 3 times in TN buffer +Tween-20, incubated for 1 h at room temperature with biotinylated 2nd antibody (1:300 in blocking buffer), washed 4 times, incubated with Streptavidin-HRP in blocking buffer, washed 3 times, incubated with Tyramide signal amplification (TSA) solution + 1μg/ml DAPI for 15 min, washed in PBS, and mounted as above.

RNAscope in situ hybridization (ISH), confocal imaging, and quantitation— Probes for RNAscope (catalog numbers in the Key Resources Table) were used as described previously (McCarthy et al., 2020a) except for 12 min target retrieval, based on the manufacturer's recommendations with the RNAscope Multiplex Fluorescent Reagent Kit v2 (ACD). After the last hybridization, additional antibody staining and mounting were performed as above for ACTA2 (abcam, ab5694) or LAMA2 (Sigma, L9393). Slides were imaged using one of two confocal microscopes: Leica Sp5 for which image processing and export were performed in LAS X Version 3.5.7.23225 (Leica Microsystems CMS GmbH); or Zeiss Lsm900 using Zeiss ZEN blue 3.5 lite software (Carl Zeiss Microscopy GmbH).

Relative fluorescence intensities were quantified in these systems, summarized in Microsoft Excel, and plotted using Prism9 (GraphPad Inc) as follows: Regions of interest (ROI) were drawn along the crypt length above the muscularis mucosae, fluorescent channel intensity was quantified using the Profile function (grid distance=10) in Zeiss ZEN blue 3.5 lite. Values were calculated as % of total distance from crypt bottoms per image (crypt bottom to top =100%). To normalize for variation in crypt length or signal brightness, for each measurement, we calculated the % of average channel fluorescence per image. Intensities were measured in at least 3 different images from 3 different $Wnt4^{CreERT2;tdTom}$ or $Grem1^{tdTom}$ mice. Values were processed in R using reshape2 and ggplot2 to plot the smoothened mean with 95% confidence interval via function (geom_smooth, method=loess).

Whole mount sample preparation— The protocol for intestinal whole-mount imaging adapted from [75] was described previously [17]. In brief, mouse tissue was perfused and fixed overnight in 4% paraformaldehyde in PBS, washed and incubated overnight in 10% sucrose +10% glycerol before blocking for 6 h and staining with anti-PDGFRA Ab (R&D Systems, AF1062) for 3 days at 4°C. After 5 washes, secondary antibody, phalloidin (Life Technologies), and DAPI were applied for 2 days at 4°C, followed by 10 washes in PBS. Small tissue sections were manually cut, cleared with FocusClear for 30 min at room temperature, and mounted in 97% Thiodiethanol (TDE) onto slides with a space holder (Grace Bio-Labs) before sealing with a coverslip.

Protein extraction and immunoblotting— Cells were lysed in RIPA buffer (Sigma) with Complete Protease Inhibitor (Roche) for 20 min at 4°C and 30 min on ice. Lysates were centrifuged at 12,000 g for 15 min at 4°C to remove cellular debris and supernatants were stored at −80°C until further use. Protein extracts were quantified using a BCA kit (Pierce). 5–7 μg protein was boiled for 5 min at 95°C in 4x Laemmli buffer (BioRad), loaded onto 5–12% gradient gels (BioRad), and electrophoresed at 100 V for 45 min in

Running buffer (BioRad). Protein was transferred onto PVDF membranes at 55 V for 90 min at 4°C in transfer buffer (BioRad) containing 10% methanol (Sigma). Phospho-Smad 1/5 (1:1000, Cell Signaling Technology, 9516) and ACTB (loading control, 1:500, Sigma, A5441) were detected with HRP-coupled secondary antibodies (Invitrogen, 656120 and 626520) and chemiluminescence products were imaged by LS Quant 4000 (GE healthcare). Signal intensities were quantified in Fiji (ImageJ 1.52p). pSMAD1/5 band intensity was normalized to that of ACTB control from the same sample lane and blot.

Data processing and analysis

Bulk RNA-sequencing: RNA-seq samples were aligned to the mm10 genome and processed using the Viper pipeline [76] with default parameters. Differential gene expression analysis was performed in R software (R Core Team (2015)) version 3.6.0 and the Bioconductor (Biobase_2.46.0, BiocParallel_1.20.1) package DESeq2 ver1.26.0 [78] using $|\log_2 FC|$ cut-off >1.5 and $P_{adj} < 0.01$. Normalized counts extracted from DEseq2 and $\log_2 FC$ values were plotted in GraphPad Prism9. Related samples were clustered by Euclidian distance, method="complete", and plotted with pHeatmap ver 1.0.12.

Single-cell RNA-sequencing: Samples were aligned to the mm10 genome using 10x Genomics Cell Ranger 3.0.2 using default parameters[79]. Bioinformatic analyses were conducted via R version 3.6.0. Single-cell analyses used Seurat_3.2.2.[80]. Cells were filtered for a minimum of 1,000 and a maximum of 3,500 reads and <5% mitochondrial reads and data were log-normalized (factor=10,000). Cell features were detected with the FindVariableFeatures function (2,000 features, selection method "vst"). The first 15 principal components were taken to run uniform manifold approximation and projection (UMAP) algorithms[81]. Cell types were identified using established marker genes detected by the "FindAllMarkers" function in Seurat2 (min.pct=0.25, test "roc"). Data from SI (sample GSM3242185 from GEO series GSE116514)[23] and colon (GSE114374, Mouse_HC_expression_matrix)[49] were processed in the same manner. Multiple samples were merged using Seurat's integration function over 2,000 features with SCT-normalization.

Some scRNA-seq data from SI were generated previously[17]: GEO accession nos. GSM4196131 and GSM4196132. Two libraries of unfractionated SI mesenchyme were processed and combined by integration in Seurat as above. As these samples had not excluded CD45+ cells, we filtered these out by *Ptprc* (*Cd45*) expression in the respective clusters. Pearson correlation was calculated in R based on AverageExpression of all *SCT*-normalized gene counts per cell type cluster and plotted with the package pheatmap_1.0.12. Exported raw RNA-seq counts from this dataset were subsequently used in cNMF analysis for the SI.

Consensus non-negative matrix factorization (cNMF): cNMF analyses were performed in a Python environment (3.7.13) using custom functions (https://github.com/wagnerde/scTools-py.git), Scrublet (0.2.3), and ScanPy (1.8.2). Colonic scRNA-seq data were filtered for cells with at least 3,000 detected transcripts, <5% mitochondrial reads, and doublet scores <0.20. cNMF analyses were performed with the cnmf package (v1.3.2) using the

prepare, factorize, combine, and consensus subroutines with n=100 iterations and n=2,000 variable genes, as described[50]. For each dataset, k values were determined empirically to maximize silhouette scores (stability) relative to the Frobenius reconstruction error through the use of a k-selection plot. The values determined for each sample were k=22 (SI, whole mesenchyme), k=18 (colon, whole mesenchyme), k=16 (SI, PDGFRA^{+} cells). UMAP plots for GEP score overlays were constructed within ScanPy using n=2,000 variable genes and n=50 principal components.

Trajectory Analysis: Expression over pseudotime (Fig. 3C) was calculated using Slingshot[48]. Graph diffusion distance-based ordering was performed on a subset of 3,370 $Pdgfra^{lo}$ cells by randomly selecting a root cell in the $Grem1^+$ trophocyte cluster and calculating the diffusion pseudotime (dpt) distance of all remaining cells relative to that root [51]. Trajectories were assembled for paths through specified clusters, with cells ordered by dpt values. Mean and SD values for select genes were plotted along sliding windows of 200 cells (Fig. 3F).

ATAC-sequencing: Reads were trimmed using trim_galore v0.4.5, using a stringency of 3 for adapter trimming and a minimum trimmed read length of 30 (Krueger et al., 2021). Alignment to the mm10 genome was done using bowtie2 v2.3.4.3 with default parameters[83]. Samtools v1.9 was used for file processing, including the removal of duplicate reads[84]. Sample quality was assessed using the RSeqQC v4.0.0 suite[85]. Peaks were called using MACS2 v2.1.1 (Feng et al., 2012), with q-value cut-off 0.001, lower Mfold=5, upper Mfold=50. Bigwig files were generated using bamCoverage from the DeepTools v3.0.2 package, with bin size of 10 bp, smoothing of 30 bp, and normalizing using reads per genomic content. Unstranded peak overlap of biological replicates was further processed excluding the mm10 blacklist. A universal peak set was obtained using the Merge tool in bedtools v2.29.0[87] to merge the peak overlap in each biological group and Bamliquidator (https://github.com/linlabcode/bamliquidator-batch) to aggregate counts within the universal peak set. The resulting matrix was used to perform a gap statistic calculation with clusGap from the cluster library in R v3.6.0, resulting in an optimal k=6. Enhancers were defined as open chromatin peak regions <1 kb and >2 kb from transcription start sites. ATAC-seq heatmaps (peak centers ±1.5 kb) were produced using the computeMatrix and plotHeatmap functions in DeepTools v3.3.2.0.1[88] using k=6.

QUANTIFICATION AND STATISTICAL ANALYSIS

Prism9 (GraphPad Inc) was used for statistical analysis of all data other than nucleotide sequences. Specific tests and significance levels are indicated in the respective figure legends. Non-parametric tests were chosen when data was not normally distributed based on D'Agostino & Pearson, Anderson-Darling, Shapiro-Wilk, and Kolmogorov-Smirnov tests with alpha=0.05. No prior determination of sample size or power calculation was performed.

Graphical illustrations were created with BioRender.com.

Supplementary Material

Refer to Web version on PubMed Central for supplementary material.

Acknowledgments

REFERENCES

1. Barker N, van Es JH, Kuipers J, Kujala P, van den Born M, Cozijnsen M, Haegebarth A, Korving J, Begthel H, Peters PJ, et al. (2007). Identification of stem cells in small intestine and colon by marker gene Lgr5. Nature 449, 1003–1007. 10.1038/nature06196. [PubMed: 17934449]

2. Barker N (2014). Adult intestinal stem cells: critical drivers of epithelial homeostasis and regeneration. Nat Rev Mol Cell Biol 15, 19–33. 10.1038/nrm3721. [PubMed: 24326621]

3. Kinzler KW, Nilbert MC, Vogelstein B, Bryan TM, Levy DB, Smith KJ, Preisinger AC, Hamilton SR, Hedge P, Markham A, et al. (1991). Identification of a gene located at chromosome 5q21 that is mutated in colorectal cancers. Science (1979) 251, 1366–1370. 10.1126/science.1848370.

4. Sato T, Vries RG, Snippert HJ, van de Wetering M, Barker N, Stange DE, van Es JH, Abo A, Kujala P, Peters PJ, et al. (2009). Single Lgr5 stem cells build crypt-villus structures in vitro without a mesenchymal niche. Nature 459, 262–265. 10.1038/nature07935. [PubMed: 19329995]

5. Sato T, Stange DE, Ferrante M, Vries RGJ, van Es JH, van den Brink S, van Houdt WJ, Pronk A, van Gorp J, Siersema PD, et al. (2011). Long-term expansion of epithelial organoids from human colon, adenoma, adenocarcinoma, and Barrett's epithelium. Gastroenterology 141, 1762–1772. 10.1053/j.gastro.2011.07.050. [PubMed: 21889923]

6. Jung P, Sato T, Merlos-Suárez A, Barriga FM, Iglesias M, Rossell D, Auer H, Gallardo M, Blasco MA, Sancho E, et al. (2011). Isolation and in vitro expansion of human colonic stem cells. Nat Med 17, 1225–1227. 10.1038/nm.2470. [PubMed: 21892181]

7. Sato T, van Es JH, Snippert HJ, Stange DE, Vries RG, van den Born M, Barker N, Shroyer NF, van de Wetering M, and Clevers H (2011). Paneth cells constitute the niche for Lgr5 stem cells in intestinal crypts. Nature 469, 415–418. 10.1038/nature09637. [PubMed: 21113151]

8. Kim T-HHT-H, Escudero S, and Shivdasani RA (2012). Intact function of Lgr5 receptor-expressing intestinal stem cells in the absence of Paneth cells. Proc Natl Acad Sci U S A 109, 3932–3937. 10.1073/pnas.1113890109. [PubMed: 22355124]

9. Durand A, Donahue B, Peignon G, Letourneur F, Cagnard N, Slomianny C, Perret C, Shroyer NF, and Romagnolo B (2012). Functional intestinal stem cells after Paneth cell ablation induced by the loss of transcription factor Math1 (Atoh1). Proc Natl Acad Sci U S A 109, 8965–8970. 10.1073/pnas.1201652109. [PubMed: 22586121]

10. Farin HF, van Es JH, and Clevers H (2012). Redundant sources of Wnt regulate intestinal stem cells and promote formation of paneth cells. Gastroenterology 143, 1518–1529.e7. 10.1053/j.gastro.2012.08.031. [PubMed: 22922422]

11. Powell DW, Adegboyega PA, di Mari JF, and Mifflin RC (2005). Epithelial cells and their neighbors: I. Role of intestinal myofibroblasts in development, repair, and cancer. Am J Physiol Gastrointest Liver Physiol 289. 10.1152/ajpgi.00075.2005.

12. Powell DW, Pinchuk IV, Saada JI, Chen X, and Mifflin RC (2011). Mesenchymal Cells of the Intestinal Lamina Propria. Annu Rev Physiol 73, 213–237. 10.1146/annurev.physiol.70.113006.100646. [PubMed: 21054163]

13. Greicius G, Kabiri Z, Sigmundsson K, Liang C, Bunte R, Singh MK, and Virshup DM (2018). *PDGFRa* $^+$ pericryptal stromal cells are the critical source of Wnts and RSPO3 for murine intestinal stem cells in vivo. Proc Natl Acad Sci U S A 115, E3173–E3181. 10.1073/pnas.1713510115. [PubMed: 29559533]

14. Kabiri Z, Greicius G, Madan B, Biechele S, Zhong Z, Zaribafzadeh H, Edison, Aliyev J, Wu Y, Bunte R, et al. (2014). Stroma provides an intestinal stem cell niche in the absence of epithelial Wnts. Development (Cambridge) 141, 2206–2215. 10.1242/dev.104976.

15. Stzepourginski I, Nigro G, Jacob J-MM, Dulauroy S, Sansonetti PJ, Eberl G, and Peduto L (2017). CD34+ mesenchymal cells are a major component of the intestinal stem cells niche at homeostasis and after injury. Proc Natl Acad Sci U S A 114, E506–E513. 10.1073/pnas.1620059114. [PubMed: 28074039]

16. Karpus ON, Westendorp BF, Vermeulen JLM, Meisner S, Koster J, Muncan V, Wildenberg ME, and van den Brink GR (2019). Colonic CD90+ Crypt Fibroblasts Secrete Semaphorins to Support Epithelial Growth. Cell Rep 26, 3698–3708.e5. 10.1016/j.celrep.2019.02.101. [PubMed: 30917322]

17. McCarthy N, Manieri E, Storm EE, Saadatpour A, Luoma AM, Kapoor VN, Madha S, Gaynor LT, Cox C, Keerthivasan S, et al. (2020). Distinct Mesenchymal Cell Populations Generate the Essential Intestinal BMP Signaling Gradient. Cell Stem Cell 26, 391–402.e5. 10.1016/j.stem.2020.01.008. [PubMed: 32084389]

18. Valenta T, Degirmenci B, Moor AE, Herr P, Zimmerli D, Moor MB, Hausmann G, Cantù C, Aguet M, Basler K, et al. (2016). Wnt Ligands Secreted by Subepithelial Mesenchymal Cells Are Essential for the Survival of Intestinal Stem Cells and Gut Homeostasis. Cell Rep 15, 911–918. 10.1016/j.celrep.2016.03.088. [PubMed: 27117411]

19. Shoshkes-Carmel M, Wang YJ, Wangensteen KJ, Tóth B, Kondo A, Massassa EE, Itzkovitz S, Kaestner KH, Massasa EE, Itzkovitz S, et al. (2018). Subepithelial telocytes are an important source of Wnts that supports intestinal crypts. Nature 557, 242–246. 10.1038/s41586-018-0084-4. [PubMed: 29720649]

20. Aoki R, Shoshkes-Carmel M, Gao N, Shin S, May CL, Golson ML, Zahm AM, Ray M, Wiser CL, Wright CVE, et al. (2016). Foxl1-Expressing Mesenchymal Cells Constitute the Intestinal Stem Cell Niche. Cell. Mol. Gastroenterol. Hepatol. 2, 175–188. 10.1016/j.jcmgh.2015.12.004. [PubMed: 26949732]

21. Deng M, Guerrero-Juarez CF, Sheng X, Xu J, Wu X, Yao K, Li M, Yang X, Li G, Xiao J, et al. (2022). Lepr + mesenchymal cells sense diet to modulate intestinal stem/progenitor cells via Leptin-Igf1 axis. Cell Res. 10.1038/S41422-022-00643-9.

22. McCarthy N, Kraiczy J, and Shivdasani RA (2020). Cellular and molecular architecture of the intestinal stem cell niche. Nat Cell Biol 22, 1033–1041. 10.1038/s41556-020-0567-z. [PubMed: 32884148]

23. Kim JE, Fei L, Yin WC, Coquenlorge S, Rao-Bhatia A, Zhang X, Shi SSW, Lee JH, Hahn NA, Rizvi W, et al. (2020). Single cell and genetic analyses reveal conserved populations and signaling mechanisms of gastrointestinal stromal niches. Nat Commun 11. 10.1038/s41467-019-14058-5.

24. Thomson CA, van de Pavert SA, Stakenborg M, Labeeuw E, Matteoli G, Mowat AM, and Nibbs RJB (2018). Expression of the Atypical Chemokine Receptor ACKR4 Identifies a Novel Population of Intestinal Submucosal Fibroblasts That Preferentially Expresses Endothelial Cell Regulators. The Journal of Immunology 201, 215–229. 10.4049/jimmunol.1700967. [PubMed: 29760193]

25. Brügger MD, Valenta T, Fazilaty H, Hausmann G, and Basler K (2020). Distinct populations of crypt-associated fibroblasts act as signaling hubs to control colon homeostasis. PLoS Biol 18, e3001032. 10.1371/journal.pbio.3001032. [PubMed: 33306673]

26. Butler A, Hoffman P, Smibert P, Papalexi E, and Satija R (2018). Integrating single-cell transcriptomic data across different conditions, technologies, and species. Nat Biotechnol 36, 411–420. 10.1038/nbt.4096. [PubMed: 29608179]

27. Buenrostro JD, Giresi PG, Zaba LC, Chang HY, and Greenleaf WJ (2013). Transposition of native chromatin for fast and sensitive epigenomic profiling of open chromatin, DNA-binding proteins and nucleosome position. Nat Methods 10, 1213–1218. 10.1038/nmeth.2688. [PubMed: 24097267]

28. Klemm SL, Shipony Z, and Greenleaf WJ (2019). Chromatin accessibility and the regulatory epigenome. Nat Rev Genet 20, 207–220. 10.1038/S41576-018-0089-8. [PubMed: 30675018]

29. Mah AT, Yan KS, and Kuo CJ (2016). Wnt pathway regulation of intestinal stem cells. J Physiol 594, 4837. 10.1113/JP271754. [PubMed: 27581568]

30. Korinek V, Barker N, Moerer P, van Donselaar E, Huls G, Peters PJ, and Clevers H (1998). Depletion of epithelial stem-cell compartments in the small intestine of mice lacking Tcf-4. Nat Genet 19, 379–383. 10.1038/1270. [PubMed: 9697701]

31. Farin HF, Jordens I, Mosa MH, Basak O, Korving J, Tauriello DVFF, de Punder K, Angers S, Peters PJ, Maurice MM, et al. (2016). Visualization of a short-range Wnt gradient in the intestinal stem-cell niche. Nature 530, 340–343. 10.1038/nature16937. [PubMed: 26863187]

32. Shimomura Y, Agalliu D, Vonica A, Luria V, Wajid M, Baumer A, Belli S, Petukhova L, Schinzel A, Brivanlou AH, et al. (2010). APCDD1 is a novel Wnt inhibitor mutated in hereditary hypotrichosis simplex. Nature 464, 1043–1047. 10.1038/NATURE08875. [PubMed: 20393562]

33. Bartscherer K, Pelte N, Ingelfinger D, and Boutros M (2006). Secretion of Wnt Ligands Requires Evi, a Conserved Transmembrane Protein. Cell 125, 523–533. 10.1016/J.CELL.2006.04.009. [PubMed: 16678096]

34. Bänziger C, Soldini D, Schütt C, Zipperlen P, Hausmann G, and Basler K (2006). Wntless, a Conserved Membrane Protein Dedicated to the Secretion of Wnt Proteins from Signaling Cells. Cell 125, 509–522. 10.1016/J.CELL.2006.02.049. [PubMed: 16678095]

35. Niec RE, Chu T, Schernthanner M, Gur-Cohen S, Hidalgo L, Pasolli HA, Luckett KA, Wang Z, Bhalla SR, Cambuli F, et al. (2022). Lymphatics act as a signaling hub to regulate intestinal stem cell activity. Cell Stem Cell. 10.1016/J.STEM.2022.05.007.

36. Goto N, Goto S, Imada S, Hosseini S, Deshpande V, and Yilmaz ÖH (2022). Lymphatics and fibroblasts support intestinal stem cells in homeostasis and injury. Cell Stem Cell 29, 1246–1261.e6. 10.1016/J.STEM.2022.06.013. [PubMed: 35931033]

37. Palikuqi B, Rispal J, Reyes EA, Vaka D, Boffelli D, and Klein O (2022). Lymphangiocrine signals are required for proper intestinal repair after cytotoxic injury. Cell Stem Cell 29, 1262–1272.e5. 10.1016/J.STEM.2022.07.007. [PubMed: 35931034]

38. Proffitt KD, and Virshup DM (2012). Precise regulation of porcupine activity is required for physiological Wnt signaling. Journal of Biological Chemistry 287, 34167–34178. 10.1074/JBC.M112.381970. [PubMed: 22888000]

39. Kolev HM, Tian Y, Kim MS, Leu NA, Adams-Tzivelekidis S, Lengner CJ, Li N, and Kaestner KH (2021). A FoxL1-CreERT-2A-tdTomato Mouse Labels Subepithelial Telocytes. Cell. Mol. Gastroenterol. Hepatol. 12, 1155–1158.e4. 10.1016/J.JCMGH.2021.05.009. [PubMed: 34029742]

40. Chung MI, Bujnis M, Barkauskas CE, Kobayashi Y, and Hogan BLM (2018). Niche-mediated BMP/SMAD signaling regulates lung alveolar stem cell proliferation and differentiation. Development 145. 10.1242/DEV.163014.

41. Muzumdar MD, Tasic B, Miyamichi K, Li N, and Luo L (2007). A global double-fluorescent Cre reporter mouse. Genesis 45, 593–605. 10.1002/DVG.20335. [PubMed: 17868096]

42. Barrott JJ, Cash GM, Smith AP, Barrow JR, and Charles Murtaugh L Deletion of mouse Porcn blocks Wnt ligand secretion and reveals an ectodermal etiology of human focal dermal hypoplasia/Goltz syndrome. 10.1073/pnas.1006437108.

43. Yang Q, Bermingham NA, Finegold MJ, and Zoghbi HY (2001). Requirement of Math1 for secretory cell lineage commitment in the mouse intestine. Science (1979) 294, 2155–2158. 10.1126/SCIENCE.1065718/SUPPL_FILE/1065718S4_THUMB.GIF.

44. Shroyer NF, Helmrath MA, Wang VYC, Antalffy B, Henning SJ, and Zoghbi HY (2007). Intestine-specific ablation of mouse atonal homolog 1 (Math1) reveals a role in cellular homeostasis. Gastroenterology 132, 2478–2488. 10.1053/J.GASTRO.2007.03.047. [PubMed: 17570220]

45. Proffitt KD, Madan B, Ke Z, Pendharkar V, Ding L, Lee MA, Hannoush RN, and Virshup DM (2013). Pharmacological inhibition of the Wnt acyltransferase PORCN prevents growth of WNT-driven mammary cancer. Cancer Res 73, 502–507. 10.1158/0008-5472.CAN-12-2258. [PubMed: 23188502]

46. Gregorieff A, Pinto D, Begthel H, Destrée O, Kielman M, and Clevers H (2005). Expression Pattern of Wnt Signaling Components in the Adult Intestine. Gastroenterology 129, 626–638. 10.1053/j.gastro.2005.06.007. [PubMed: 16083717]

47. Yan KS, Janda CY, Chang J, Zheng GXYY, Larkin KA, Luca VC, Chia LA, Mah AT, Han A, Terry JM, et al. (2017). Non-equivalence of Wnt and R-spondin ligands during Lgr5 + intestinal stem-cell self-renewal. Nature 545, 238–242. 10.1038/nature22313. [PubMed: 28467820]

48. Street K, Risso D, Fletcher RB, Das D, Ngai J, Yosef N, Purdom E, and Dudoit S (2018). Slingshot: Cell lineage and pseudotime inference for single-cell transcriptomics. BMC Genomics 19. 10.1186/S12864-018-4772-0.

49. Kinchen J, Chen HH, Parikh K, Antanaviciute A, Jagielowicz M, Fawkner-Corbett D, Ashley N, Cubitt L, Mellado-Gomez E, Attar M, et al. (2018). Structural Remodeling of the Human Colonic Mesenchyme in Inflammatory Bowel Disease. Cell 175, 372–386.e17. 10.1016/j.cell.2018.08.067. [PubMed: 30270042]

50. Kotliar D, Veres A, Nagy MA, Tabrizi S, Hodis E, Melton DA, and Sabeti PC (2019). Identifying gene expression programs of cell-type identity and cellular activity with single-cell RNA-Seq. Elife 8. 10.7554/eLife.43803.

51. Haghverdi L, Büttner M, Wolf FA, Buettner F, and Theis FJ (2016). Diffusion pseudotime robustly reconstructs lineage branching. Nature Methods 2016 13:10 13, 845–848. 10.1038/nmeth.3971.

52. Kobayashi A, Valerius MT, Mugford JW, Carroll TJ, Self M, Oliver G, and McMahon AP (2008). Six2 Defines and Regulates a Multipotent Self-Renewing Nephron Progenitor Population throughout Mammalian Kidney Development. Cell Stem Cell 3, 169–181. 10.1016/J.STEM.2008.05.020. [PubMed: 18682239]

53. Madisen L, Zwingman TA, Sunkin SM, Oh SW, Zariwala HA, Gu H, Ng LL, Palmiter RD, Hawrylycz MJ, Jones AR, et al. (2010). A robust and high-throughput Cre reporting and characterization system for the whole mouse brain. Nat Neurosci 13, 133–140. 10.1038/NN.2467. [PubMed: 20023653]

54. Jasso GJ, Jaiswal A, Varma M, Laszewski T, Grauel A, Omar A, Silva N, Dranoff G, Porter JA, Mansfield K, et al. (2022). Colon stroma mediates an inflammation-driven fibroblastic response controlling matrix remodeling and healing. PLoS Biol 20, e3001532. 10.1371/JOURNAL.PBIO.3001532. [PubMed: 35085231]

55. Sunter JP, Wright NA, and Appleton DR (1978). Cell population kinetics in the epithelium of the colon of the male rat. Virchows Arch B Cell Pathol 26, 275–287. 10.1007/BF02889556. [PubMed: 416589]

56. Cheng H, and Bjerknes M (1985). Whole population cell kinetics and postnatal development of the mouse intestinal epithelium. Anat Rec 211, 420–426. 10.1002/AR.1092110408. [PubMed: 3993991]

57. Clevers H, Loh KM, and Nusse R (2014). An integral program for tissue renewal and regeneration: Wnt signaling and stem cell control. Science (1979) 346, 1248012–1248012. 10.1126/science.1248012.

58. Qi Z, Li Y, Zhao B, Xu C, Liu Y, Li H, Zhang B, Wang X, Yang X, Xie W, et al. (2017). BMP restricts stemness of intestinal Lgr5 + stem cells by directly suppressing their signature genes. Nat Commun 8, 13824. 10.1038/ncomms13824. [PubMed: 28059064]

59. Pinto D, Gregorieff A, Begthel H, and Clevers H (2003). Canonical Wnt signals are essential for homeostasis of the intestinal epithelium. Genes Dev 17, 1709–1713. 10.1101/gad.267103. [PubMed: 12865297]

60. Kuhnert F, Davis CR, Wang HT, Chu P, Lee M, Yuan J, Nusse R, and Kuo CJ (2004). Essential requirement for Wnt signaling in proliferation of adult small intestine and colon revealed by adenoviral expression of Dickkopf-1. Proc Natl Acad Sci U S A 101, 266–271. 10.1073/pnas.2536800100. [PubMed: 14695885]

61. Degirmenci B, Valenta T, Dimitrieva S, Hausmann G, and Basler K (2018). GLI1-expressing mesenchymal cells form the essential Wnt-secreting niche for colon stem cells. Nature 558, 449–453. 10.1038/s41586-018-0190-3. [PubMed: 29875413]

62. Roulis M, Kaklamanos A, Schernthanner M, Bielecki P, Zhao J, Kaffe E, Frommelt L-S, Qu R, Knapp MS, Henriques A, et al. (2020). Paracrine orchestration of intestinal tumorigenesis by a mesenchymal niche. Nature 580, 524–529. 10.1038/s41586-020-2166-3. [PubMed: 32322056]

63. McCarthy N, Tie G, Madha S, Ruiyang H, Kraiczy J, Maglieri A, and Shivdasani R (2023). Smooth muscle contributes to the development and function of a layered intestinal stem cell niche. Dev Cell. 10.2139/SSRN.4149949.

64. Kobayashi H, Gieniec KA, Wright JA, Wang TCT, Asai N, Mizutani Y, Lida T, Ando R, Suzuki N, Lannagan TRM, et al. (2021). The Balance of Stromal BMP Signaling Mediated

by GREM1 and ISLR Drives Colorectal Carcinogenesis. Gastroenterology 160, 1224–1239.e30. 10.1053/j.gastro.2020.11.011. [PubMed: 33197448]

65. Bahar Halpern K, Massalha H, Zwick RK, Moor AE, Castillo-Azofeifa D, Rozenberg M, Farack L, Egozi A, Miller DR, Averbukh I, et al. (2020). Lgr5+ telocytes are a signaling source at the intestinal villus tip. Nat Commun 11. 10.1038/s41467-020-15714-x.

66. Haramis APG, Begthel H, van den Born M, van Es J, Jonkheer S, Offerhaus GJA, and Clevers H (2004). De Novo Crypt Formation and Juvenile Polyposis on BMP Inhibition in Mouse Intestine. Science (1979) 303, 1684–1686. 10.1126/science.1093587.

67. Walton KD, and Gumucio DL (2020). Hedgehog Signaling in Intestinal Development and Homeostasis. Annual Review of Physiology Annu. Rev. Physiol 2021 83, 359–380. 10.1146/annurev-physiol-031620.

68. Chee YC, Pahnke J, Bunte R, Adsool VA, Madan B, and Virshup DM (2018). Intrinsic Xenobiotic Resistance of the Intestinal Stem Cell Niche. Dev Cell 46, 681–695.e5. 10.1016/j.devcel.2018.07.023. [PubMed: 30146480]

69. Hamilton TG, Klinghoffer RA, Corrin PD, and Soriano P (2003). Evolutionary Divergence of Platelet-Derived Growth Factor Alpha Receptor Signaling Mechanisms. Mol Cell Biol 23, 4013–4025. 10.1128/mcb.23.11.4013-4025.2003. [PubMed: 12748302]

70. Wirth A, Benyó Z, Lukasova M, Leutgeb B, Wettschureck N, Gorbey S, Rsy PO+, Horváth B, Maser-Gluth C, Greiner E, et al. (2008). G 12-G 13-LARG-mediated signaling in vascular smooth muscle is required for salt-induced hypertension. 10.1038/nm1666.

71. Srinivas S, Watanabe T, Lin CS, William CM, Tanabe Y, Jessell TM, and Costantini F (2001). Cre reporter strains produced by targeted insertion of EYFP and ECFP into the ROSA26 locus. BMC Dev Biol 1, 1–8. 10.1186/1471-213X-1-4. [PubMed: 11178105]

72. el Marjou F, Janssen KP, Chang BHJ, Li M, Hindie V, Chan L, Louvard D, Chambon P, Metzger D, and Robine S (2004). Tissue-specific and inducible Cre-mediated recombination in the gut epithelium. Genesis 39, 186–193. 10.1002/gene.20042. [PubMed: 15282745]

73. Buenrostro JD, Wu B, Chang HY, and Greenleaf WJ (2015). ATAC-seq: A Method for Assaying Chromatin Accessibility Genome-Wide. Curr Protoc Mol Biol 109, 21.29.1–9. 10.1002/0471142727.mb2129s109.

74. Jadhav U, Cavazza A, Banerjee KK, Xie H, O'Neill NK, Saenz-Vash V, Herbert Z, Madha S, Orkin SH, Zhai H, et al. (2019). Extensive Recovery of Embryonic Enhancer and Gene Memory Stored in Hypomethylated Enhancer DNA. Mol Cell 74, 542–554.e5. 10.1016/j.molcel.2019.02.024. [PubMed: 30905509]

75. Bernier-Latmani J, Cisarovsky C, Demir CS, Bruand M, Jaquet M, Davanture S, Ragusa S, Siegert S, Dormond O, Benedito R, et al. (2015). DLL4 promotes continuous adult intestinal lacteal regeneration and dietary fat transport. Journal of Clinical Investigation 125, 4572–4586. 10.1172/JCI82045. [PubMed: 26529256]

76. Cornwell MI, Vangala M, Taing L, Herbert Z, Köster J, Li B, Sun H, Li T, Zhang J, Qiu X, et al. (2018). VIPER: Visualization Pipeline for RNA-seq, a Snakemake workflow for efficient and complete RNA-seq analysis. BMC Bioinformatics 19. 10.1186/S12859-018-2139-9.

77. Team, R.C. R Core Team (2015). R: A language and environment for statistical computing. R Foundation for Statistical Computing, Vienna, Austria. URL https://www.R-project.org/.

78. Love MI, Huber W, and Anders S (2014). Moderated estimation of fold change and dispersion for RNA-seq data with DESeq2. Genome Biol 15, 550. 10.1186/s13059-014-0550-8. [PubMed: 25516281]

79. Zheng GXY, Terry JM, Belgrader P, Ryvkin P, Bent ZW, Wilson R, Ziraldo SB, Wheeler TD, Mcdermott GP, Zhu J, et al. (2017). ARTICLE Massively parallel digital transcriptional profiling of single cells. Nat Commun. 10.1038/ncomms14049.

80. Stuart T, Butler A, Hoffman P, Hafemeister C, Papalexi E, Mauck WM, Hao Y, Stoeckius M, Smibert P, and Satija R (2019). Comprehensive Integration of Single-Cell Data. Cell 177, 1888–1902.e21. 10.1016/j.cell.2019.05.031. [PubMed: 31178118]

81. McInnes L, and Healy J (2018). UMAP: Uniform Manifold Approximation and Projection for Dimension Reduction. 10.21105/joss.00861.

82. Krueger F, James F, Ewels P, Afyounian E, and Schuster-Boeckler B (2021). FelixKrueger/ TrimGalore: v0.6.7 - DOI via Zenodo. 10.5281/ZENODO.5127899.

83. Langmead B, and Salzberg SL (2012). Fast gapped-read alignment with Bowtie 2. Nat Methods 9, 357–359. 10.1038/nmeth.1923. [PubMed: 22388286]

84. Danecek P, Bonfield JK, Liddle J, Marshall J, Ohan V, Pollard MO, Whitwham A, Keane T, McCarthy SA, Davies RM, et al. (2021). Twelve years of SAMtools and BCFtools. Gigascience 10, 1–4. 10.1093/GIGASCIENCE/GIAB008.

85. Wang L, Wang S, and Li W (2012). RSeQC: Quality control of RNA-seq experiments. Bioinformatics 28, 2184–2185. 10.1093/BIOINFORMATICS/BTS356. [PubMed: 22743226]

86. Feng J, Liu T, Qin B, Zhang Y, and Liu XS (2012). Identifying ChIP-seq enrichment using MACS. Nat Protoc 7, 1728–1740. 10.1038/nprot.2012.101. [PubMed: 22936215]

87. Quinlan AR, and Hall IM (2010). BEDTools: A flexible suite of utilities for comparing genomic features. Bioinformatics 26, 841–842. 10.1093/bioinformatics/btq033. [PubMed: 20110278]

88. Ramírez F, Ryan DP, Bj¨ B, Grüning B, Grüning G, Bhardwaj V, Kilpert F, Richter AS, Heyne S, Undar FD¨, et al. (2016). deepTools2: a next generation web server for deep-sequencing data analysis. Web Server issue Published online 44. 10.1093/nar/gkw257.

Highlights

- In addition to CD81$^+$ trophocytes, other PDGFRA^{lo} cells support intestinal stem cells

- The CD81$^-$ fraction of PDGFRA^{lo} cells is a principal source of canonical Wnt ligands

- These cells segregate along the crypt length into niche-active and inert fractions

- Distance from a BMP signaling center organizes that spatially segregated niche
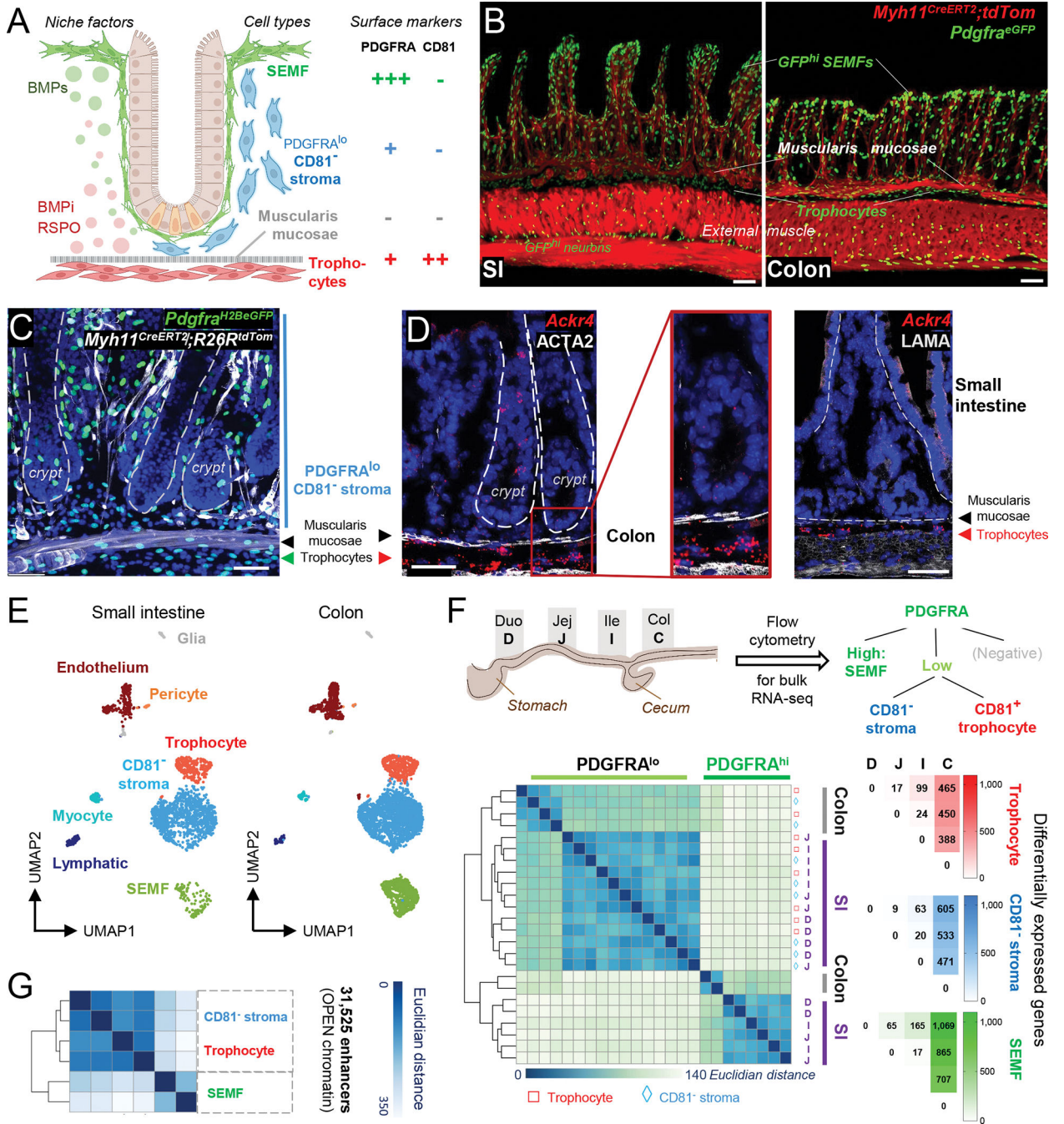
Figure 1. Relationship of mesenchymal cell populations across the intestinal length.

A) Cell populations and signaling in SI crypts. BMPi provided by sub-cryptal trophocytes (red, PDGFRA^{lo} CD81^{+}) oppose agonists provided by dense SEMF (green, PDGFRA^{hi}) aggregates at the crypt-villus junction. The function of supra-muscularis PDGFRA^{lo} cells (blue), which lack CD81 expression, is unknown and is the topic of this study.

B) Confocal images of *Myh11^{CreERT2};R26R$^{LSL-tdTom}$;Pdgfra^{H2BeGFP}* mouse ileum (SI, left, 24 μm z-stack) and colon (right, 15 μm z-stack). Scale bars 50 μm.

C) Left, whole-mount confocal micrograph (26-μm z-stack) of colonic tissue from *Pdgfra^H2B-eGFP*;*Myh11^CreERT2*;*R26R^tdTom* mice. White: *Myh11^Cre*-marked smooth muscle, green: GFP$^+$ nuclei, blue (DAPI): cell nuclei. Dashed lines demarcate crypts. Scale bar 50 μm.

D) In situ hybridization for trophocyte marker *Ackr4* (red) in colonic crypts counterstained with ACTA2 antibody (white). Rare epithelial *Ackr4*$^+$ cells are tuft cells. Dashed lines demarcate crypts. Scale bars 50 μm.

E) scRNAseq-derived UMAP clustering of unfractionated SI (n=2,042)[17] and colonic (n=3,940) EPCAM$^-$ CD45$^-$ mesenchymal cell types identified using known cell-specific markers (Figure S1B).

F) Differential PDGFRA and CD81 expression allow purification of 3 dominant PDGFRA$^+$ cell types from each intestinal segment: duodenum (D), jejunum (J), ileum (I), and colon (C). Left, Unsupervised hierarchical clustering of duplicate bulk RNA-seq profiles of SEMFs (green), trophocytes (red), and CD81$^-$ stromal cells (blue) from each intestinal segment; the latter two populations cluster together. Color scale: Euclidean distance of samples. Right, Numbers of differentially expressed genes (P_{adj}<0.01, log$_2$ fold-difference >|1.5|) in each cell type and intestinal segment.

G) Hierarchical clustering of duplicate PDGFRA$^+$ cell samples from whole SI by similarities in open chromatin reads (ATAC-Seq) at the union set of 31,525 enhancers (> −1 kb, > 2 kb from transcription start sites). Color scale: Euclidean distance.
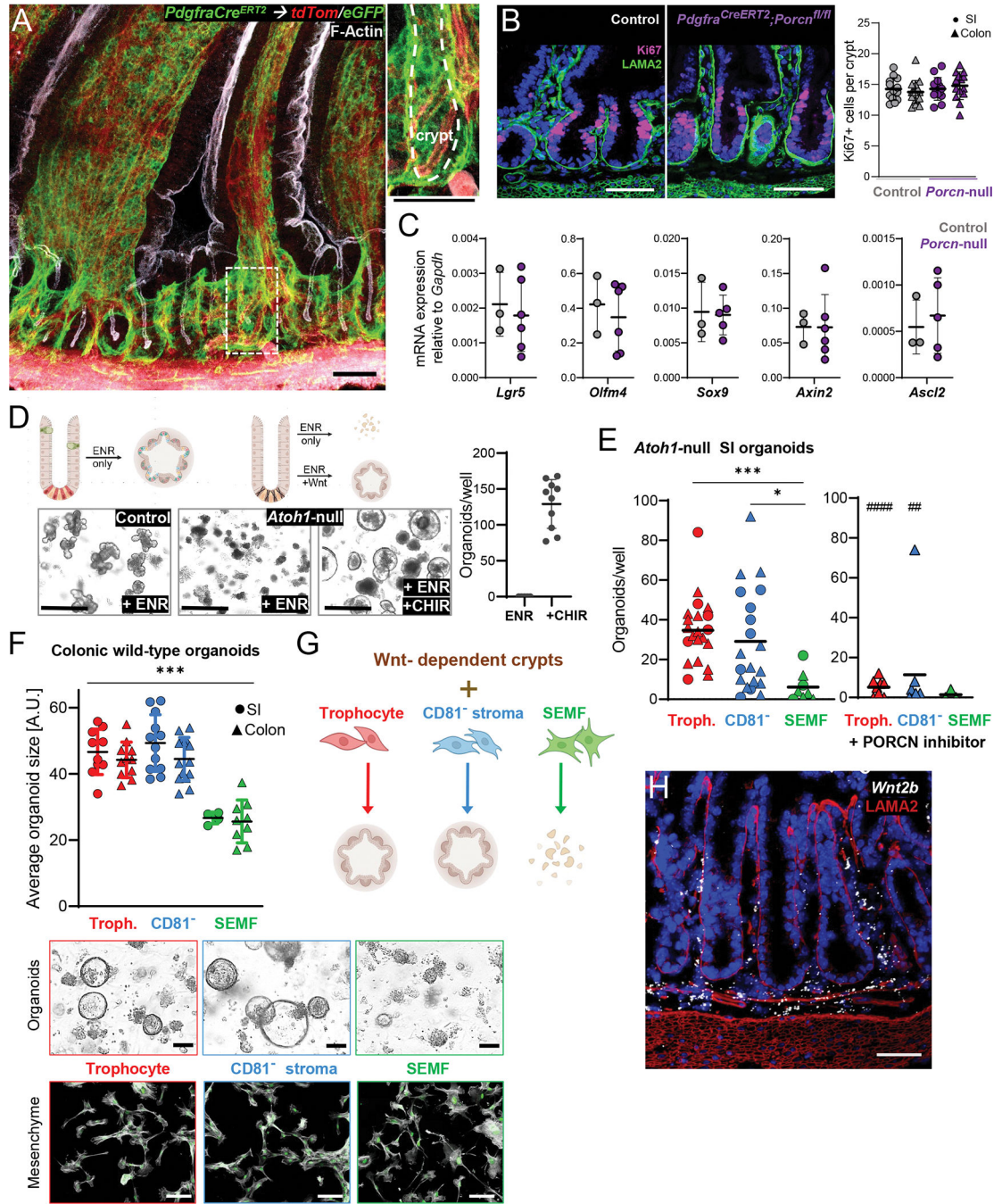
See also Figure S1.

Figure 2. PDGFRA^{lo} intestinal cells are a key source of canonical Wnts.

A) Whole-mount images of SI from *Pdgfra^{CreERT2};R26R$^{mT/mG}$* mice, where Cre-expressing cells convert ubiquitous tdTom fluorescence (red) to eGFP signal (green), counterstained for F-Actin (phalloidin, white). 30 μm z-stack overlay. The dashed box is enlarged to the right and the crypt in that image is marked with a dashed white line. Scale bars 50 μm.

B) Ki67 immunofluorescence (magenta) in control (left) and *Pdgfra^{CreERT2};Porcn$^{fl/fl}$* mouse (*Porcn-null*) SI after 5 daily tamoxifen injections and 10 days recovery, counterstained for laminin (LAMA2, green) and nuclei (DAPI, blue). Representative images and quantitation

of Ki67$^+$ stained cells in SI (circles) and colonic (triangles) crypts from n=4 (control) and n=6 (*Porcn*-null) animals. At least 10 crypts per sample counted. Lines indicate Mean ±SD.

C) mRNA expression of ISC-associated marker genes in crypt epithelium isolated from control (left, n=3) and *Porcn*-null (right, n=6) mice 10 days after 5 daily tamoxifen injections, measured by quantitative real-time PCR and expressed relative to *Gapdh* levels (2$^{-\Delta Ct}$). Lines indicate Mean ±SD. Additional makers are shown in Figure S3F.

D) Exogenous Wnt requirement for organoid growth from *Atoh1*-null SI crypts. Representative brightfield images of organoids from control (*Atoh1*$^{fl/fl}$) or *Atoh1*-null (*Vil1-Cre*^{ERT2};*Atoh1*$^{fl/fl}$) SI crypts grown in ENR medium only or with the GSK3 inhibitor CHIR99021 (CHIR). Scale bar 200 μm. Right, *Atoh1*-null organoid numbers per 10 μl Matrigel droplet on the 4th day of culture. Each dot represents one sample, lines indicate Mean ±SD, n=4 independent experiments.

E) Organoid counts from *Atoh1*-null SI crypts cultured in ENR with duodenal (circles) or colonic (triangles) mesenchymal cells (10,000 cells per 10 μl Matrigel droplet) 4 days after plating without (left graph) or with (right graph) 100 nM Wnt-C59, a Porcupine inhibitor. Each dot represents one sample, lines indicate mean counts from 5 independent experiments. Kruskal-Wallis ANOVA, SEMFs vs. trophocytes P_{adj} 0.0004 (***); SEMF vs. CD81$^-$ stroma cells P_{adj} 0.0016 (*). Comparisons of the same cell type with or without Wnt-C59 were made using the Mann-Whitney test, P_{adj} 0.008 (##), P_{adj}<0.0001 (###).

F) Organoid size 4 days after wild-type colonic crypts were co-cultured with mesenchymal cells (2,000 cells per 10 μl Matrigel droplet in ENR medium) isolated from SI (circles) or colon (triangles). Values are in arbitrary units (A.U.) and lines indicate Mean ±SD. P_{adj} <0.0005 (***) for any trophocyte or CD81$^-$ stromal cell sample vs. any SEMF sample (one-way ANOVA, Tukey- corrected). Micrographs: Top row, representative bright-field images of organoids from colonic crypts cultured with the indicated colonic mesenchymal cell type. Bottom row, corresponding mesenchymal cells on day 4 of co-culture, showing Pdgfra^{eGFP} expression (green) and F-Actin (phalloidin, grey) counterstain as indicators of cell viability. Scale bars 50μm.

G) Summary of experimental results from panels E and F.

H) *Wnt2b* in situ hybridization (white) in colon tissue sections counterstained with laminin antibody (LAMA2, red) and DAPI (blue). Scale bar 50 μm. Representative image from n= 4 mice. Additional images are shown in Figure S4F.

See also Figures S2–S4.
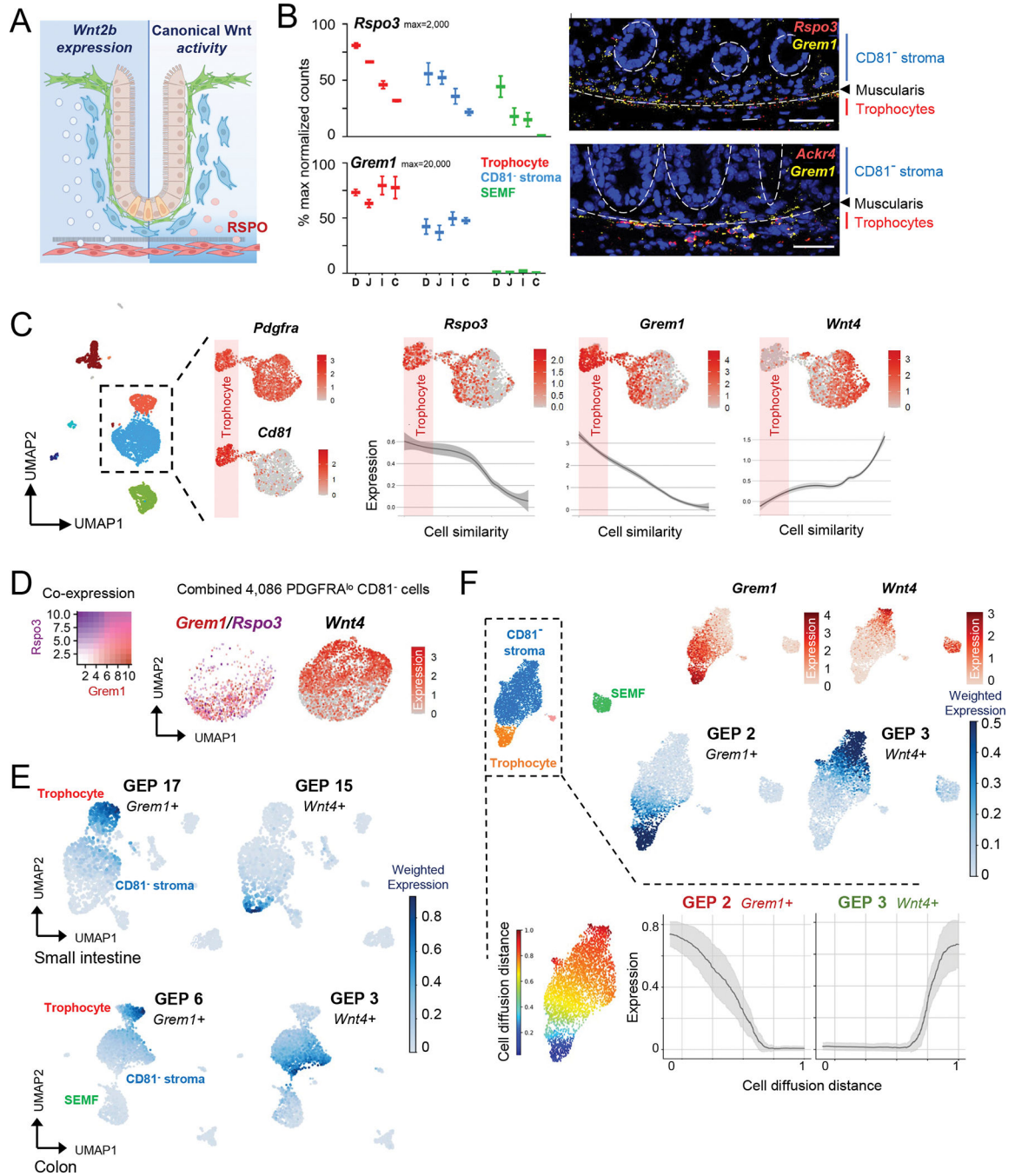
Figure 3. Molecular heterogeneity of CD81⁻ stromal cells.

A) Model for *Wnt2b* expression domain (left, broad) and predicted signal activity (right, spatially restricted by RSPO localization).

B) Left, normalized bulk RNA-seq counts for *Rspo3* and *Grem1* in PDGFRA⁺ cells from each intestinal region. n=2 biological replicates per cell type and region. Right, in situ hybridization of colonic tissue for *Rspo3* (red - top), *Grem1* (yellow), and *Ackr4* (red - bottom) counterstained with DAPI (blue). Scale bars 50 μm. Dashed circles: crypts, dashed lines: muscularis mucosae.

C) Feature plots of selected markers in scRNA-seq analysis of *Pdgfra^lo* cells extracted *in silico* from whole mesenchyme data (Fig. 1E, n=2,472); *Cd81* marks trophocytes. *Rspo3*, *Grem1*, and *Wnt4* expression is quantified below in Pdgfra^lo cells ranked (pseudotime algorithm) by similarity to trophocytes (shaded in pink). Expression means are smoothened and shaded regions on the curves represent the 95% confidence interval.

D) *Grem1 and Rspo3* (overlay, left) and *Wnt4* (right) expression on an aggregate feature plot from all 4,086 Pdgfra^lo CD81⁻ cells. In addition to those extracted in silico as above, these include cells from 2 independent replicates (CD81⁻ fractions of 1,184 cells and 865 cells, respectively) purified by *Pdgfra^eGFP* flow cytometry.

E) Consensus non-negative matrix factorization (cNMF)-based average expression of gene expression programs (GEPs) containing *Grem1* (module 17 in SI, module 6 in colon) or *Wnt4* (GEP 15 in SI, GEP 3 in colon) among the top-weighted genes.

F) scRNA-seq feature plots for *Grem1* and *Wnt4* in 3,370 isolated from wild-type mice by flow cytometry using PDGFRA antibody. Leiden clusters identified by known marker genes (see Fig. S1B) are shown alongside feature plots for *Grem1* and *Wnt4* (top) and cNMF plots for the modules that contain these markers (middle) and below a map of color-coded cell diffusion distances along the *Pdgfra^lo* subset, calculated by diffusion pseudotime[51] relative to trophocytes as the root. Moving average expression and standard deviation (grey) are shown for GEPs 2 (*Grem1*⁺) and 3 (*Wnt4*⁺), calculated using a sliding window of 200 cells and ordered by diffusion distance (0=most similar; 1=most different).

See also Figure S5.
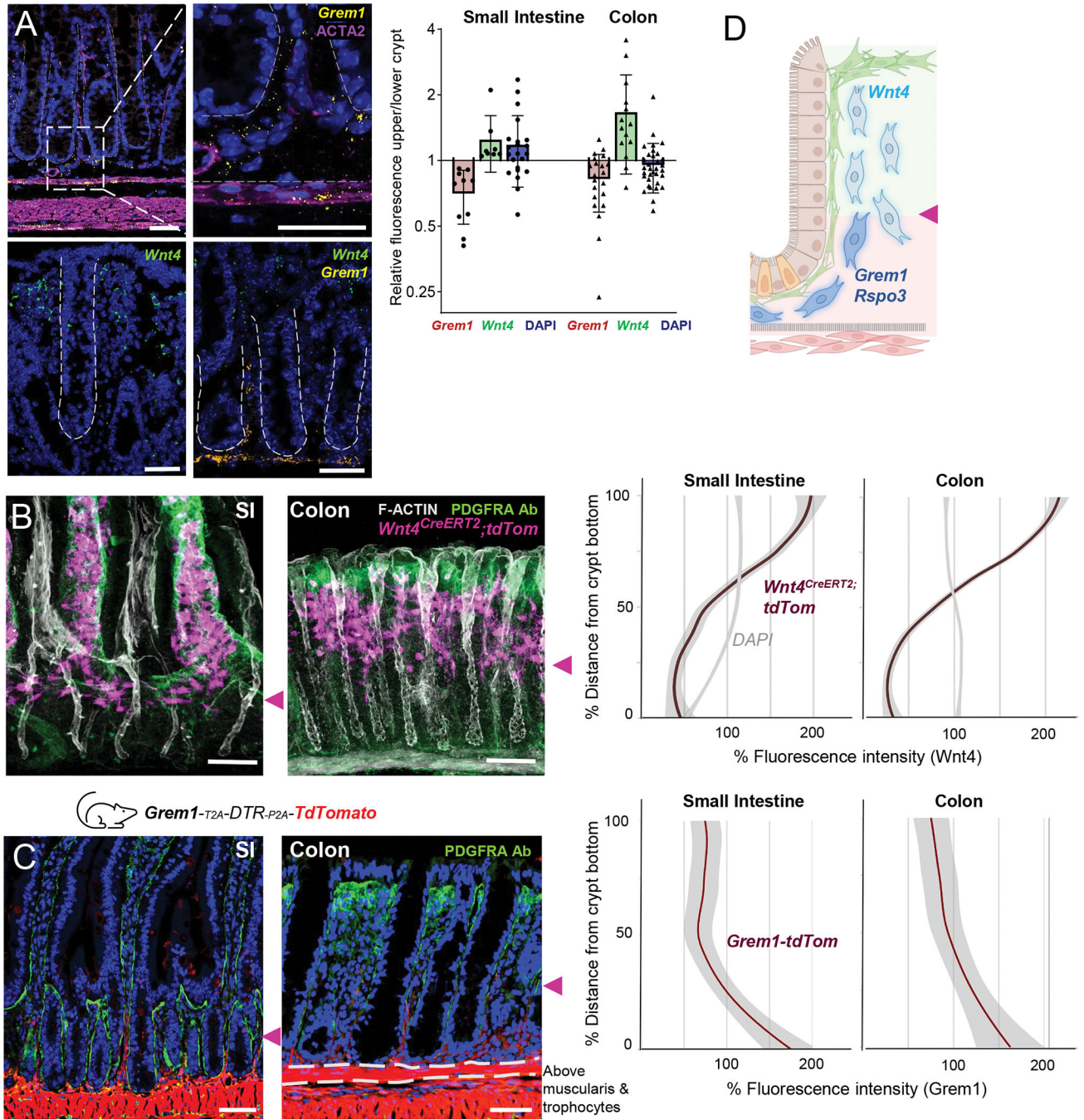
Figure 4. Spatial segregation of heterogenous CD81⁻ stromal cells.

A) *Grem1* and *Wnt4* ISH in colon, stained with ACTA2 Ab (magenta in *Grem1* ISH) or both probes together. Graph: ratios of RNAscope fluorescence intensity for each marker in sub-epithelial cells in the upper (luminal) and lower (serosal) crypt halves (equal measurement areas, mean fluorescence measured above the muscularis mucosae, DAPI signals control for cell density). Each dot represents one image measurement, sampled across multiple tissue sections from n=3 animals.

B) *Wnt4* expression detected by the tdTom fluorescence proxy in *Wnt4^{CreERT2};R26R^{tdTom}* SI (left) and colon (right) 2 weeks after tamoxifen injection. Tissue whole-mounts were counterstained with PDGFRA Ab to highlight SEMFs (green), phalloidin to demarcate boundaries (F-Actin, white), and DAPI (blue). Confocal 40-μm z-stacks are shown; see Figure S6C for single cross-sections without phalloidin staining. Scale bars 50 μm. Purple arrowheads point to lower edges of the *Wnt4*$^+$ stromal domain. Graphs quantify the percent of average tdTom (red line) and DAPI (grey line) fluorescence intensity along the length from crypt bottom (0) to crypt top (100: full crypt length). The graphs display smoothened mean values with 95% confidence interval (shaded grey) from n=3 mice.

C) SI and colonic tissue sections from *Grem1*^{tdTom} (red) reporter mice, stained with PDGFRA antibody (green) and DAPI (nuclei, blue). Dashed lines indicate muscularis mucosae. Purple arrowheads point to upper edges of the *Grem1*$^+$ stromal domain. Scale bars 50 μm. Graphs quantify average tdTom fluorescence (red line) along the crypt, from bottom (0) to top (100), as in panel B. The graphs display smoothened mean values with 95% confidence interval (shaded grey) from n=3 mice.

D) Schema of heterogeneous CD81$^−$ PDGFRA^{lo} cell states along the crypt axis marked by factor expression. Cell symbols as in Fig. 1.
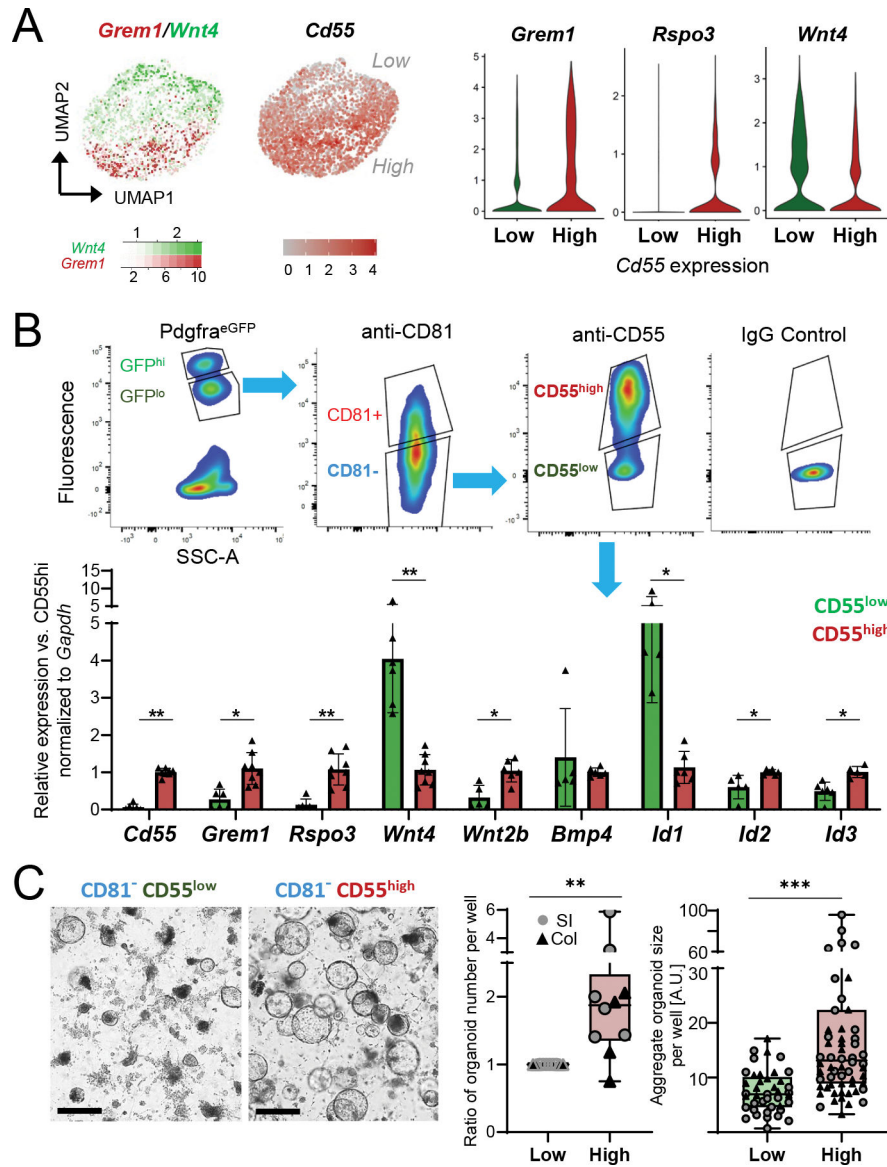
See also Figure S6.

Figure 5. Functional distinction of heterogenous CD81⁻ stromal cells.

A) Left, *Grem1* (red) and *Wnt4* (green) expression overlay and *Cd55* levels in single *Cd81⁻* stromal cells aggregated from independent collections, as in Figure 3D. Right, marker expression in scRNA-seq data in cells separated *in silico* for high (SCT-transformed counts >1, n= 1,756 cells) or low (n=2,322 cells) *Cd55* expression.

B) Top, representative side-scatter area (SSC-A) and fluorescence plots from FACS isolation of PDGFRA^{lo} (based on native *Pdgfra^{eGFP}* signal) CD81⁻ (fluorophore-conjugated 2nd Ab) cells with high or low surface CD55 expression (conjugated Ab, FACS gating with IgG isotype control). Below, qRT-PCR for selected mRNAs in primary colonic PDGFRA^{lo} CD81⁻ stromal cells sorted for low (green) or high (red) surface CD55. mRNA expression is normalized to *Gapdh* and displayed relative to average expression in CD55^{hi} cells (C$_t$). Bars: Mean ±SD from n=5–8 independent cell isolations.

C) Organoids from duodenal crypts co-cultured with CD55^{lo} or CD55^{hi} cells without added growth factors 4 days after seeding at 10,000 stromal cells/10 μl Matrigel droplet; brightfield images, scale bars 200 μm. Left graph shows fold-difference of average organoid *number* per well 4 days after the start of co-culture with CD55^{hi} cells, relative to CD55^{lo} cell co-culture (=1). Each point represents the organoid count (average of biological replicates) from each independent experiment with stromal cells from SI (circles, n=6 experiments) or colon (triangles, n=4 experiments). Two-tailed Wilcoxon matched-pairs signed rank test, ***P*$_{adj}$ 0.006. Right graph shows the sum of all organoid diameters per well in arbitrary units (A.U.) from the same experiments. Box: 25th-75th percentile with median, whiskers: minimum to maximum values. Two-tailed Mann-Whitney test, ***P*$_{adj}$ <0.001.
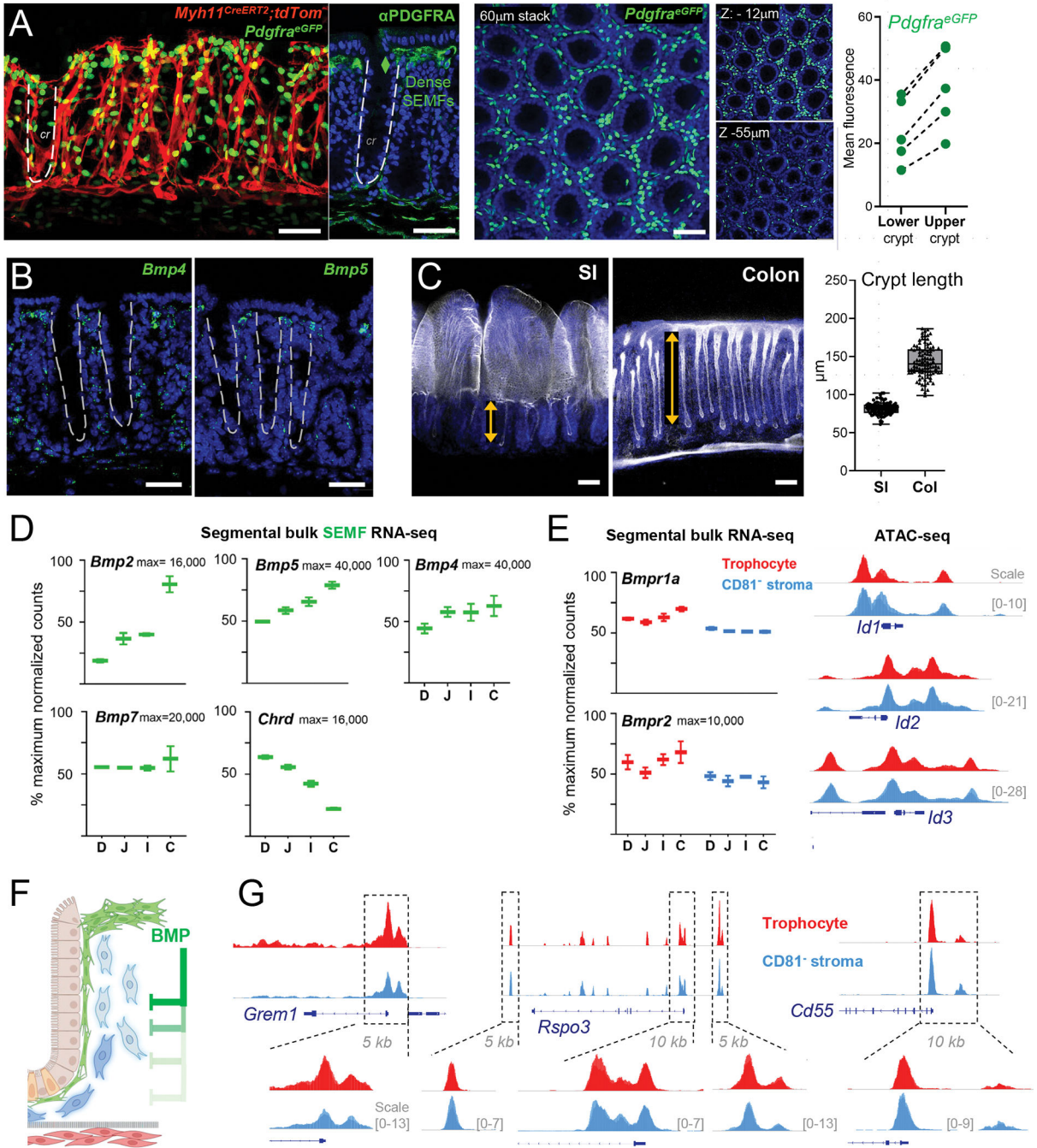
Figure 6. BMPs as candidates for intra-mesenchymal signaling in crypt niche zonation

A) Left: $Myh11^{CreERT2};R26R^{tdTom};Pdgfra^{eGFP}$ mouse colon showing SEMF (PDGFRA^hi cells, 60 µm stack, *en face* view) distribution along the crypt length demarcated by tdTom^+ myocytes. Adjacent image shows a z-slice of the same tissue stained with PDGFRA Ab (green) and DAPI (nuclei, blue); the dashed line demarcates one crypt. Center, Whole-mount confocal microscopy of colonic $Pdgfra^{eGFP}$ crypts counterstained with DAPI (blue). A 60-µm stack is shown with 6-µm sub-stacks at z= −9 to −15 µm (top) and z= −52 to −58 µm (below) shown alongside. Right, eGFP signals were quantified in crypt upper and lower

halves as mean fluorescence values in cross-sections of whole-mount images (5 images each from n=3 mice); lines connect paired values from each image. All scale bars 50 μm.

B) In situ hybridization (RNAscope, green) for *Bmp4* and *Bmp5* in adult mouse colon sections co-stained with DAPI (blue). Dashed lines demarcate crypts. Scale bars 50 μm.

C) Whole-mount confocal images of SI and colon after stripping external smooth muscle layers and staining with phalloidin (F-actin, white) and DAPI (blue). SI: single whole-mount micrograph, colon: 60-μm z-stack. Double arrows outline crypt heights and the graph depicts the heights of 200 crypts measured on tissue sections from n=3 wild-type adult mice stained with hematoxylin and eosin (see Figure S7D).

D) Normalized bulk RNA-seq counts for BMP ligands and the BMPi *Chordin* (*Chrd*) in SEMFs from each intestinal segment: duodenum (D), jejunum (J), ileum (I), and colon (C) from n=2 mice. Y-axis: percent of maximum normalized read counts (as indicated) for each gene. Box: 25th- 75th percentile, whiskers: minimum to maximum values.

E) Left, normalized bulk RNA-seq counts of BMP receptors 1a and 2 *(Bmpr1a and Bmpr2)* in SI and colonic trophocytes and CD81⁻ stromal cells (both max=10,000 read counts). *Bmpr1b* mRNA was not detected. Right, IGV tracks of open chromatin (ATAC-seq signals overlaid from duplicate SI samples) at BMP-responsive loci *Id1*, *Id2*, and *Id3* (10-kb regions, y-axis scales as indicated).

F) Schema of the hypothesis that BMPs from SEMF aggregates at crypt tops restrain the niche properties of PDGFRA^lo cells. BMP-mediated gene suppression is relieved with increasing distance from those aggregates, allowing PDGFRA^lo cells toward the crypt bottom to express niche factors and functions.

G) IGV tracks (ATAC-seq signal overlay from duplicate samples) from PDGFRA^lo mesenchymal cells at the *Grem1*, *Rspo3*, and *Cd55* loci. Boxed 5–10 kb regions are magnified to highlight trophocyte and CD81⁻ stromal cell similarities. Y-axis scales are indicated.

See also Figure S7.
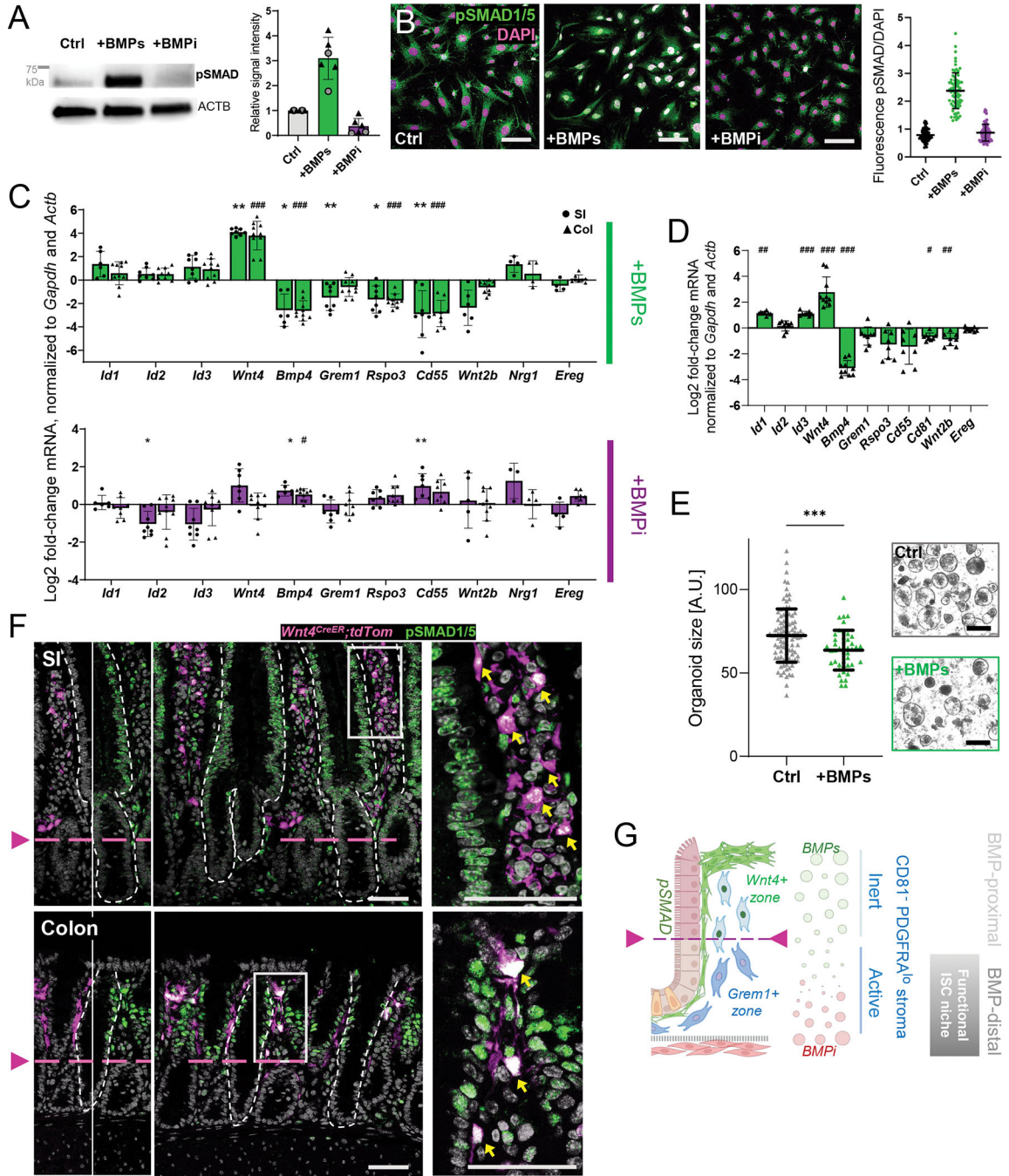
Figure 7. BMP-responsive gene regulation in CD81⁻ stromal cells

A) Phospho-SMAD1/5 and ACTB (loading control of the same lane) immunoblots from cultured PDGFRA^{lo} CD81⁻ CD55^{hi} stromal cells treated for 5 days with rBMP2/4/7 (100 ng/mL each, combined) or BMPi (rGREM1 and rNOG, 100 ng/mL each, combined) in serum-free medium. The position of a 75-kDa size marker is indicated. Graph: pSMAD1/5 chemiluminescence signals quantified relative to ACTB in SI (circles) or colonic (triangles) cells with respect to untreated cells (Ctrl). Bars represent the Mean±SD from n=6 independent blots.

B) pSMAD1/5 immunofluorescence (green) in cultured PDGFRA^{lo} CD81$^-$ CD55^{hi} stromal cells after treatment with rBMPs or rBMPi. Scale bars 100 μm. Representative images from n=4 independent cell isolations and experiments. Graph: nuclear pSMAD fluorescence intensity normalized to DAPI signals. Each dot represents one cell. Lines= Mean ±SD.

C) qRT-PCR assessment of selected transcripts after treatment of primary SI (circles) and colonic (triangles) PDGFRA^{lo} CD81$^-$ CD55^{hi} stromal cells for 5 days with rBMPs (top) or rBMPi (bottom) in serum-free media. Expression was normalized to *Gapdh* and *Actb* RNA levels. Results are represented as log_2 fold-change of normalized expression compared to control cultures of the same region (C_t). Bar graphs: Mean ±SD of individual samples, derived from n=4 (SI) or n=5 (colon) experiments with 1–2 biological replicates per experiment. Two-tailed Mann-Whitney test with Holm-Sidak correction, SI: P_{adj} <0.05 (*), P_{adj} <0.01 (**), colon: P_{adj} <0.05 (#), P_{adj} <0.01 (##), P_{adj} <0.001 (###).

D) qRT-PCR data for colonic trophocytes cultured and treated as in Figure 7C. Bar graphs: Mean ±SD of individual samples, derived from n=4 experiments with 2 biological replicates per experiment. Two-tailed Mann-Whitney test with Holm-Sidak correction, P_{adj} <0.05 (#), P_{adj} <0.01 (##), P_{adj} <0.001 (###).

E) Organoid size 4 days after SI crypts were co-cultured with PDGFRA^{lo} CD81$^-$ CD55^{hi} stromal cells (10,000 cells/10 μl Matrigel) pre-treated for 5 days with rBMP2/4/7 (+BMPs) or untreated (Ctrl, serum-free medium only). Values are in arbitrary units (A.U.) and lines indicate mean±SD. Data are collated from n=3 independent experiments (1–3 biological replicates in each; the individual experiments are shown in Figure S7E) and each value represents one organoid. Unpaired t-test with Welch-correction P_{adj}=0.0004 (***).

F) pSMAD1/5 immunofluorescence (green) and native tdTom signal (magenta) in *Wnt4$^{eGFP-CreERT2)}$;R26R^{tdTom}* mouse SI (top) and colon (bottom). Left, Single-color view of overlay image in the center. Arrowheads and dashed magenta lines indicate the lower pSMAD/Wnt4 expression boundary. Dashed white lines demarcate epithelium from mesenchyme. Right, magnified insets of boxed areas, with yellow arrows pointing to pSMAD$^+$ (nuclear signal) Wnt4$^+$ (cytoplasmic signal) stromal cells. Scale bars 50 μm.

G) Model for BMP signaling, with supra-cryptal SEMFs providing BMP ligands that are opposed by sub-cryptal BMPi sources, as one basis for heterogenous PDGFRA^{lo} stromal cell states and consequent self-organization of the ISC niche.

See also Figure S7.

Key Resource Table

REAGENT or RESOURCE	SOURCE	IDENTIFIER
Antibodies		
AlexaFluor 594 donkey anti-goat IgG	Invitrogen	A11058
AlexaFluor Goat 546 anti-rat IgG	Invitrogen	A11081
AlexaFluor Goat 633 anti-rabbit IgG	Invitrogen	A21071
Alpha-smooth muscle actin	Abcam	5694; RRID: AB_2223021
Armenian Hamster IgG Isotype Control	eBioscience	eBio299Arm
Beta-Actin	Sigma	A5441
CD31	BD	557355; RRID: AB_396660
CD34	BioLegend	119310
CD45-APC	invitrogen	17045182
CD55 clone RIKO-3	BioLegend	131803
CD81-biotin Clone EAT2	eBioscience	13-0811-81
EpCAM-PE clone G8.8	eBioscience	12-5791-83
GFP	Abcam	6556/6662RRIDs: AB_305564 and AB_305635
Goat anti-mouse IgG HRP conjugate	Invitrogen	62-6520
Goat anti-rabbit IgG HRP-conjugate	Invitrogen	656120
Laminin	Sigma	L9393; RRID: AB_477163
Lysozyme	Dako	A0099; RRID: AB_2341230
MKi67	Invitrogen	MA5-14520
Pdgfra (IHC)	R&D Systems	AF1062; RRID: AB_2236897
Pdgfra (CD140a-Ab) for FACS	BioLegend	135905
PE Armenian Hamster IgG Isotype Ctrl	BioLegend	400907
Phospho-Smad 1/5(ser463/465) (41D10) Rabbit mAb	Cell Signaling Technology	9516 RRID: AB_491015
Streptavidin-APC	eBioscience	17431782
anti-rabbit biotinylated 2nd antibody	Jackson Immuno Research	111-065-003
Streptavidin-HRP	Jackson Immuno Research	016-030-084
Tyramide-C3	Perkin Elmer	NEL744E001KT
Chemicals, peptides, and recombinant proteins		
Agarose	A1705Z	Azura Genomics
Alexa Fluor 647 Phalloidin	Life Technologies	A22287
AMPure beads	Beckman Coulter	A63880
B-27 Supplement (50X)	Life Technologies	17504001
Blocking Reagent	Perkin Elmer	FP1020
Bovine Serum Albumin	Sigma	A9647
CHIR99021 (Chir)	Sigma-Aldrich	SML1046-5MG
Chlorophorm	Sigma-Aldrich	C2432
Collagenase II	Worthington	LS004176

REAGENT or RESOURCE	SOURCE	IDENTIFIER
Collagenase XI	Sigma	C7657
Complete (Protease Inhibitor Cocktail Tablets)	Sigma Aldrich	11697498001
DAPI	BD PharMingen	5649097
DAPI solution	BD Bioscience	564907
Dispase II	Sigma	D4693
Dulbecco's Modified Eagle Medium (DMEM)	Corning	17-205-CV
DMEM/F12 Media	GIBCO	12634-010
EDTA	Gibco	AM9260G
Fetal Bovine Serum	Corning	35-010-CV
FocusClear	CelExplorer	FC-101
Glutamax	GIBCO	35050-661
Hanks' Balanced Salt Solution (HBSS, 10X)	GIBCO	14065-056
HEPES	Sigma	H3375
30% H2O2	Electron Microscopy Science	2621-02
Matrigel	Corning	356231
Mini-Protean TGX Gels	BioRad	4561084
N-2 Supplement (100X)	Life Technologies	17502001
N-Acetylcysteine	Sigma	A9165
Normal Goat Serum	Cell Signaling	5425S
Paraformaldehyde	EMS	15714-S
PBS (10X)	Corning	46-013-CM
Penicillin/Streptomycin	Life Technologies	15140163
Pierce Bovine Serum Albumin Standard Ampules	Life Technologies	23209
Recombinant EGF	ThermoFisher	PHG0311
Recombinant Gremlin-1	ThermoFisher	956GR050
Recombinant Human/Murine/Rat BMP-2	Peprotech	120-02C-10UG
Recombinant Murine BMP-4	Peprotech	315-27-10UG
Recombinant Murine BMP-7	R&D	5666-BP/CF
Recombinant Noggin	Peprotech	120-10C
Sodium azide	Sigma	S2002
T ransfer Buffer (10x)	Boston BioProducts	BP-190
Tris-Glycine-SDS Running buffer (10x)	Boston BioProducts	BP-150
Triton X-100	Sigma	T8787
Trizol reagent	ThermoFisher	15596026
T rypLE Express	Thermo Fisher Scientific	12604-021
Trypsin 0.25% EDTA	Life Technologies	25200114
VectaShield mounting medium	Vector Laboratories	H-1000
Wnt-C59	ThermoFisher	NC0186427
Critical commercial assays		

REAGENT or RESOURCE	SOURCE	IDENTIFIER
BCA PROTEIN ASSAY KIT	Thermo Fisher	PI23227
Agilent High Sensitivity DNA Kit	Agilent	5067-4626
Agilent RNA 6000 Pico Kit	Agilent	NoImage 5067-1513
Alcian Blue Counterstain	Thermo Fisher	NC1318236
Chromium Next GEM Chip G Single Cell Kit	10X Genomics	PN-1000120
Chromium Next GEM Single Cell 3' GEM, Library & Gel Bead Kit v3.1, 4 rxns PN-1000128	10X Genomics	PN-1000128
DNA-purification kit	Qiagen	28004
ECL Prime Western Blotting Detection Reagents	GE Healthcare	RPN2232
High-Fidelity 2X PCR master mix	New England Biolabs	M0541S
Nextera Tn5 Transposase	Illumina	FC-121-1030
Power SYBR Green PCR MasterMix	Life Technologies	4367659
PureLink RNA mini kit	Life Technologies	12183018A
Qubit dsDNA high-sensitivity assay	Life Technologies	Q32851
RNAscope Hydrogen Peroxide	ACD	322335
RNAscope Multiplex Fluorescent Reagent Kit v2	ACD	323100
RNAscope Protease III	ACD	322337
RNeasy Plus micro kit	Qiagen	74034
SapphireAmp Fast PCR Mastermix	Takara	RR350
Single Index Kit T Set A	10X Genomics	PN-100021
SMART-Seq v4 Ultra Low Input RNA kit	Clontech	634890
SUPERSCRIPT III 1ST STRAND	Life Technologies	18080051
Deposited data		
Bulk RNA-seq mesenchymal cells	This study	GEO accession: GSE211275
ATAC-seq mesenchymal cells	This study	GEO accession: GSE211275
scRNA-seq whole mesenchyme colon	This study	GEO accession: GSE211275
scRNA-seq PdgfraLow cells colon	This study	GEO accession: GSE211275
scRNA-seq Pdgfra+ cells small intestine	This study	GEO accession: GSE212601
scRNA-seq whole mesenchyme small Intestine	McCarthy et al	GEO: GSE130681 GSM4196131, GSM4196131
scRNA-seq whole mesenchyme colon	Kinchen et al	GEO: GSE114374
scRNA-seq whole mesenchyme small Intestine	Kim et al	GEO: GSE116514
Mouse reference genome Mm10, GRCm38	Genome Reference Consortium	https://www.ncbi.nlm.nih.gov/grc/mouse
Experimental models: Organisms/strains		
Atoh1fl/fl (B6.129S7-Atoh1tm3Hzo/J)	The Jackson Laboratory	008681 RRID:IMSR_JAX:008681
FoxL1-CreERT2-2A-tdTomato (B6.Cg-Foxl1tm2(cre/ERT2)Khk)	The Jackson Laboratory	RRID: MMRRC_068163-JAX
Grem1tdTom (Grem1-P2A-DTR-P2A-TdTomato)	This study	
Wnt4-CreERT2 (B6.Cg-Wnt4tm2(EGFP/cre/ERT2)Amc/J)	The Jackson Laboratory	032489 RRID: IMSRJAX:032489
Myh11-CreERT2 (B6.FVB-Tg(Myh11-icre/ERT2)1Soff/J)	The Jackson Laboratory	19079 RRID:IMSR_JAX:019079
PdgfraCreERT2 B6.129S-Pdgfratm1.1(cre/ERT2)Blh/J	The Jackson Laboratory	032770 RRID:IMSR_JAX:032770

REAGENT or RESOURCE	SOURCE	IDENTIFIER
PdgfraH2BeGFP (B6.129S4-Pdgfra^tm11(EGFP)Sor^/J)	The Jackson Laboratory	007669 RRID:IMSR_JAX:007669
Porcn^Fl	L. Charles Murtaugh, University of Utah, United States	
Rosa26-TdTomato B6.Cg-Gt(ROSA)26Sortm9(CAG-tdTomato)Hze/J	The Jackson Laboratory	007909 RRID:IMSR_JAX:007909
Rosa mT/mG (B6.129(Cg)-Gt(ROSA)26Sortm4(ACTB-tdTomato,-EGFP)Luo/J)	The Jackson Laboratory	007676 RRID:IMSR_JAX:007676
Rosa26-EYFP (B6.129X1-Gt(ROSA)26Sortm1(EYFP)Cos/J)	The Jackson Laboratory	006148 RRID:IMSR_JAX:006148
Vil1-Cre(ER-T2)	Sylvie Robine, Institut Pasteur, Paris, France	
Oligonucleotides		
RNAscope® Ackr4 probes	ACD	1081831
RNAscope® Bmp4 probes	ACD	454301
RNAscope® Bmp5 probes	ACD	401241
RNAscope® Grem1 probes	ACD	314741
RNAscope® Olfm4 probes	ACD	311831
RNAscope® Rspo3 probes	ACD	483781
RNAscope® Sfrp1 probes	ACD	404981
RNAscope® Wnt2b probes	ACD	405031
RNAscope® Wnt4 probes	ACD	401101
Software and algorithms		
Cell Ranger v2.1.1	10X Genomics	https://support.10xgenomics.com/single-cell-gene-expression/software/pipelines/latest/installation
BioRender		BioRender.com
cnmf v1.3.2	Kotliar et al., 2019	https://github.com/dylkot/cNMF
Corrplot	Wei et al., 2017	https://github.com/taiyun/corrplot
DeepTools	Ramírez et al., 2016	https://github.com/deeptools/deepTools
DESeq2_1.26.0	Love et al., 2014	https://bioconductor.org/packages/release/bioc/html/DESeq2.html
Diffusion Pseudotime (dpt)	Haghverdi et al., 2016	https://www.nature.com/articles/nmeth.3971
Fiji (ImageJ 1.52p)	Schindelin et al., 2012	https://imagej.net/Fiji/
FlowJo v10.6	BD Biosciene	
ggplot2_3.3.2	Wickham H., 2016	ggplot2: Elegant Graphics for Data Analysis. Springer-Verlag New York. ISBN 978-3-319-24277-4, https://ggplot2.tidyverse.org
GraphPad Prism	GraphPad, Inc	
Integrated Genomics Viewer, ver 2.9.4	Robinson et al., 2011	http://software.broadinstitute.org/software/igv/
LAS X Version 3.5.7.23225	Leica Microsystems CMS GmbH	
MAST algorithm	Finak et al., 2015	https://github.com/RGLab/MAST

REAGENT or RESOURCE	SOURCE	IDENTIFIER
Morpheus	Broad Institute	https://software.broadinstitute.org/morpheus/
Python functions for scRNA-seq	Wager Lab, UCSF	DOI: 10.5281/zenodo.7686568
R software for statistical computing	R Development Core Team, 2013	https://cran.r-project.org/bin/windows/
RSeQC	Wang et al., 2012	http://rseqc.sourceforge.net/
RStudio	RStudio Team (2020).	RStudio: Integrated Development for R. RStudio, PBC, Boston, MA URL http://www.rstudio.com
Seurat_3.2.2	Butler et al., 2018	https://github.com/satijalab/seurat
slingshot_1.4.0	Street et al., 2018	https://bioconductor.org/packages/release/bioc/html/slingshot.html
STAR	Dobin et al., 2013	https://github.com/alexdobin/STAR/releases
t-SNE algorithm	van der Maaten, 2014	https://lvdmaaten.github.io/tsne/
VIPER	Cornwell et al., 2018	https://bitbucket.org/cfce/viper/
Zen blue 3.5 (Zen lite) Version 3.5.093	Carl Zeiss Microscopy GmbH	
Other		
ACD HybEZ II Hybridization System	ACD	321710
10X Genomics Controller	10X Genomics	1000204
Leica cryostat	Leica Microsystems	CM-1510-3
Slide Spacers	Grace Bio-Labs	654002